

Validation of a Node-Centered Wall Function Model for the Unstructured Flow Code FUN3D

Jan-René Carlson*, Veer N. Vatsa[†] and Jeffery White[†]

NASA Langley Research Center, Hampton, VA

In this paper, the implementation of two wall function models in the Reynolds averaged Navier-Stokes (RANS) computational fluid dynamics (CFD) code FUN3D is described. FUN3D is a node centered method for solving the three-dimensional Navier-Stokes equations on unstructured computational grids. The first wall function model, based on the work of Knopp et al., is used in conjunction with the one-equation turbulence model of Spalart-Allmaras. The second wall function model, also based on the work of Knopp, is used in conjunction with the two-equation $k-\omega$ turbulence model of Menter. The wall function models compute the wall momentum and energy flux, which are used to weakly enforce the wall velocity and pressure flux boundary conditions in the mean flow momentum and energy equations. These wall conditions are implemented in an implicit form where the contribution of the wall function model to the Jacobian are also included. The boundary conditions of the turbulence transport equations are enforced explicitly (strongly) on all solid boundaries. The use of the wall function models is demonstrated on four test cases: a flat plate boundary layer, a subsonic diffuser, a 2D airfoil, and a 3D semi-span wing. Where possible, different near-wall viscous spacing tactics are examined. Iterative residual convergence was obtained in most cases. Solution results are compared with theoretical and experimental data for several variations of grid spacing. In general, very good comparisons with data were achieved.

*Aerospace Engineer, Computational AeroSciences Branch, MS 128, Senior Member.

[†]Aerospace Engineer, Computational AeroSciences Branch, MS 128, Associate Fellow.

I. Introduction

The increasing size of numerical simulations of steady and unsteady aerodynamic flows demands faster and more efficient computational methods to better use available resources. Robust and compact numerical schemes can reduce computational time and memory requirements. A reduction in computing requirements can also be achieved through solving a smaller problem by using models that make simplifying physical assumptions that reduce the grid resolution requirements in certain regions of the flow.

Historically, the log-law of the wall for turbulent flows has been used to construct a wall function model, which is then used to significantly reduce the grid resolution requirements in the immediate vicinity of walls. This reduction in the required wall grid resolution is achieved because the first grid point off the wall can be located in the log-law region of the boundary layer, $25 < y^+ < 250$, instead of the viscous sub-layer, $y^+ \leq 1$, where y^+ is a scaled wall-normal coordinate or wall units. The wall function is used to provide the wall momentum flux and wall energy flux to the Navier-Stokes equations; and can be used in conjunction with any number of turbulence modeling strategies from linear eddy viscosity models, hybrid RANS/LES¹ or DES.²

However, the practical application of log-law wall function models to complex flows has some challenges, the most notable of which is the difficulty of knowing where to place the first grid point off the wall when generating the grid. In complex flows and/or geometries, the state of the boundary layer is not known a priori making it difficult to generate a grid such that a log-law wall function treatment is well posed everywhere in the computational domain. A more practical approach would be to adapt the grid such that the first point off the wall is always located at a y^+ that makes the use of the wall function well posed. However, another shortcoming of log-law wall function models is that they are not valid when the wall shear stress becomes zero, for example points of flow separation or re-attachment. Therefore a wall function model that adapts to the physics of the flow local to the wall is desired. Esch et al.,³ Menter et al.,⁴ Kalitzin et al.⁵ and Knopp et al.⁶ have developed and demonstrated wall function models that blend viscous sub-layer function models and log-law function models together such that the resulting hybrid wall function model is more universal and thus, well posed for practical values of y^+ , e.g., $0 < y^+ < 250$. Moreover, Knopp et al.⁶ have demonstrated the use of this approach in conjunction with a near wall grid adaptation scheme.

The objective of this paper is to describe the implementation of the hybrid wall function models of Knopp et al.⁶ in the node-based unstructured-grid CFD code FUN3D and compare their accuracy relative to theory and relative to solutions without a wall function model for several flows of interest. The first section will discuss the turbulence and wall function models, followed by the implementation of the wall function in FUN3D, test case descriptions and a discussion of the results.

II. Turbulence and wall models

The turbulence models of Spalart-Allmaras^{7,8} and Menter et al.,⁹ are used in conjunction with the wall function approach published by Knopp et al.⁶ Both of these turbulence models are well established with the aerospace community and have been used to simulate flow around a wide variety of geometries and flow situations.

A. Spalart-Allmaras One-Equation Model

The original one-equation model of Spalart-Allmaras is given by Eq. 1,

$$\frac{\partial}{\partial t} \tilde{\nu} + \nabla(\vec{U} \tilde{\nu}) = c_{b1}(1 - f_{t2})\tilde{S}\tilde{\nu} - \left[c_{w1}f_w - \frac{c_{b1}}{\kappa^2}f_{t2} \right] \left(\frac{\tilde{\nu}}{d} \right)^2 + \frac{1}{\sigma} [\nabla \cdot ((\nu + \tilde{\nu}) \nabla \tilde{\nu}) + c_{b2} \nabla \tilde{\nu} \cdot \nabla \tilde{\nu}] \quad (1)$$

where the turbulent eddy viscosity is

$$\mu_t = \rho \tilde{\nu} f_{v1}, \quad f_{v1} = \frac{\chi^3}{\chi^3 + c_{v1}^3}, \quad \chi = \frac{\tilde{\nu}}{\nu}. \quad (2)$$

This study also used a modified form of the Spalart-Allmaras model.¹⁰ The modified model is the same as the original version except for when the turbulence variable $\tilde{\nu}$ is negative. In the situation of non-positive

values, Eq. 3 is solved instead.

$$\frac{\partial}{\partial t} \tilde{\nu} + \nabla(\vec{U} \tilde{\nu}) = c_{b1}(1 - c_{t3})|\mathbf{W}| \tilde{\nu} + c_{w1} \left(\frac{\tilde{\nu}}{d} \right)^2 + \frac{1}{\sigma} [\nabla \cdot ((\nu + \tilde{\nu} f_n) \nabla \tilde{\nu}) + c_{b2} \nabla \tilde{\nu} \cdot \nabla \tilde{\nu}] \quad (3)$$

with

$$f_n = \frac{c_{n1} + \chi^3}{c_{n1} - \chi^3}, \quad c_{n1} = 16, \quad \chi = \frac{\tilde{\nu}}{\nu} \quad (4)$$

The resulting turbulent eddy viscosity (μ_t) is set to zero when $\tilde{\nu}$ is negative ($\tilde{\nu}$ itself becomes a passive scalar). Other model parameters are defined as follows:

$$\tilde{S} = |\mathbf{W}| + \frac{\tilde{\nu}}{\kappa^2 d^2} f_{v2}, \quad f_{v2} = 1 - \frac{\chi}{1 + \chi f_{v1}} \quad (5)$$

$$|\mathbf{W}| = \sqrt{2W_{ij}W_{ij}}, \quad W_{ij} = \frac{1}{2} \left(\frac{\partial u_i}{\partial x_j} - \frac{\partial u_j}{\partial x_i} \right) \quad (6)$$

$$f_w = g \left[\frac{1 + c_{w3}^6}{g^6 + c_{w3}^6} \right]^{1/6}, \quad g = r + c_{w2}(r^6 - r), \quad r = \min \left[\frac{\tilde{\nu}}{\tilde{S} \kappa^2 d^2}, 10 \right], \quad f_{t2} = c_{t3} \exp(-c_{t4} \chi^2) \quad (7)$$

The constants are:

$$c_{b1} = 0.1355, \quad \sigma = 2/3, \quad c_{b2} = 0.622, \quad \kappa = 0.41 \quad (8)$$

$$c_{w2} = 0.3, \quad c_{w3} = 2, \quad c_{v1} = 7.1, \quad c_{t3} = 1.2, \quad c_{t4} = 0.5 \quad (9)$$

$$c_{w1} = \frac{c_{b1}}{\kappa^2} + \frac{1 + c_{b2}}{\sigma} \quad (10)$$

B. Menter-SST Two-equation model

The two-equation model used in this paper is the model proposed by Menter.⁹ Eqs. 11 and 12 are the transport equations written in conserved variable form.

$$\frac{\partial}{\partial t}(\rho k) + \nabla \cdot (\rho \vec{U} k) = P_k - \beta^* \rho \omega k + \nabla \cdot [(\mu + \sigma_k \mu_t) \nabla k] \quad (11)$$

$$\frac{\partial}{\partial t}(\rho \omega) + \nabla \cdot (\rho \vec{U} \omega) = P_k \frac{\gamma}{\nu_t} - \beta \rho \omega^2 + \nabla \cdot [(\mu + \sigma_\omega \mu_t) \nabla \omega] + 2(1 - F_1) \frac{\rho \sigma_\omega 2}{\omega} \nabla k \cdot \nabla \omega \quad (12)$$

The production of turbulent kinetic energy is stress-based

$$P_k = \tau_{ij} \frac{\partial u_i}{\partial x_j}, \quad \tau_{ij} = 2\mu_t \left(S_{ij} - \frac{1}{3} \text{tr}\{\mathbf{S}\} \delta_{ij} \right) - \frac{2}{3} \rho k \delta_{ij}, \quad S_{ij} = \frac{1}{2} \left(\frac{\partial u_i}{\partial x_j} + \frac{\partial u_j}{\partial x_i} \right) \quad (13)$$

$$P_k = \min(P_k, 10 \beta^* \rho \omega k) \quad (14)$$

with the turbulent eddy viscosity computed from:

$$\mu_t = \frac{\rho a_1 k}{\max(a_1 \omega, |\mathbf{W}| F_2)}, \quad F_2 = \tanh(\Gamma_2^2), \quad \Gamma_2 = \max \left(\frac{\sqrt{k}}{\beta^* \omega d}, \frac{500 \nu}{d^2 \omega} \right) \quad (15)$$

Each of the constants, σ_k , σ_ω , γ and β , are a blend of an inner (1) and outer (2) constant, blended via: $\phi = F_1 \phi_1 + (1 - F_1) \phi_2$ where ϕ_1 represents constant 1 and ϕ_2 represents constant 2. Additional functions are given by:

$$F_1 = \tanh(\Gamma_1^4), \quad \Gamma_1 = \min \left[\max \left(\frac{\sqrt{k}}{\beta^* \omega d}, \frac{500 \nu}{d^2 \omega} \right), \frac{4 \rho \sigma_\omega 2 k}{\text{CD}_{k\omega} d^2} \right] \quad (16)$$

$$CD_{k\omega} = \max \left(2\rho\sigma_{\omega 2} \frac{1}{\omega} \nabla k \nabla \omega, 10^{-20} \right) \quad (17)$$

The turbulent variable boundary conditions are:

$$\omega_{\text{wall}} = 10 \frac{6\nu_1}{\beta_1 d_1^2}, \quad k_{\text{wall}} = 0 \quad (18)$$

The constants are:

$$\begin{aligned} \sigma_{k1} &= 0.85, & \sigma_{k2} &= 1.0 \\ \sigma_{\omega 1} &= 0.5, & \sigma_{\omega 2} &= 0.856 \\ \gamma_1 &= 5/9, & \gamma_2 &= 0.44 \\ \beta_1 &= 0.075, & \beta_2 &= 0.0828 \\ \beta^* &= 0.09, & \kappa &= 0.41, \quad a_1 = 0.31 \end{aligned}$$

Further discussions of these models can be found on the turbulence model resource website.^{11,12}

C. Wall function model

The wall function model proposed by Knopp et al.⁶ involves two general steps to compute the friction velocity, $u_{\tau}|_{\text{wf}}$. In the first step, transcendental solutions for the friction velocity using the canonical equation of the log-law, Eq. 19, and the law-of-the-wall equation by Reichardt,¹³ Eq. 20, are blended using a hyperbolic tangent function, Eq. 21.

Equations 19 and 20 are shown in Fig. 1, as the dashed and dashed-dot curves respectively. As reference, the horizontal brace shows possible wall spacings for use with the wall function model, ranging from less than one to approximately 500. We see that Reichardt's equation already matches the viscous sub-layer quite closely, as seen by the overlap of the solid and the dashed-dot curves.

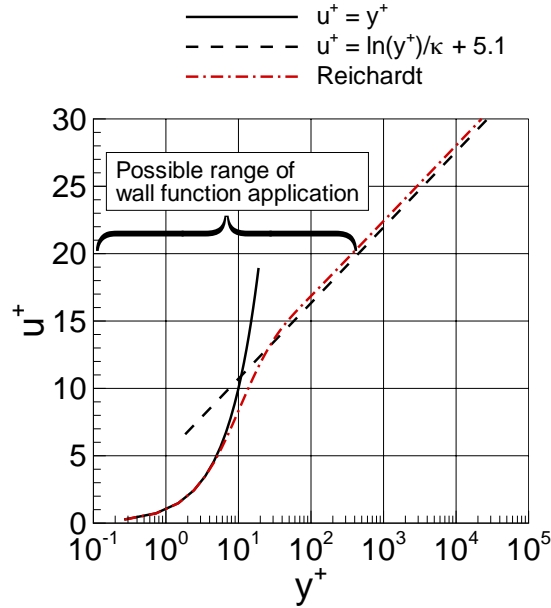


Figure 1: Canonical boundary layer profiles.

$$u_{\tau}|_{\text{Log}} \Rightarrow u_1^+ = \frac{1}{\kappa} \ln(y_1^+) + 5.1. \quad (19)$$

$$u_{\tau}|_{\text{Reichardt}} \Rightarrow u_1^+ = \frac{\ln(1 + 0.4y_1^+)}{\kappa} + 7.8 \left(1 - e^{-y_1^+/11} - \frac{y_1^+}{11} e^{-y_1^+/3} \right) \quad (20)$$

The resulting blended model, Reichardt,m, shown as the dashed-dot curve in Fig. 2(a), overlays both the sub-layer and the log-layer regions. For reference, the hyperbolic tangent blending function, φ_{b1} , is plotted along side the blended wall function, in the same figure.

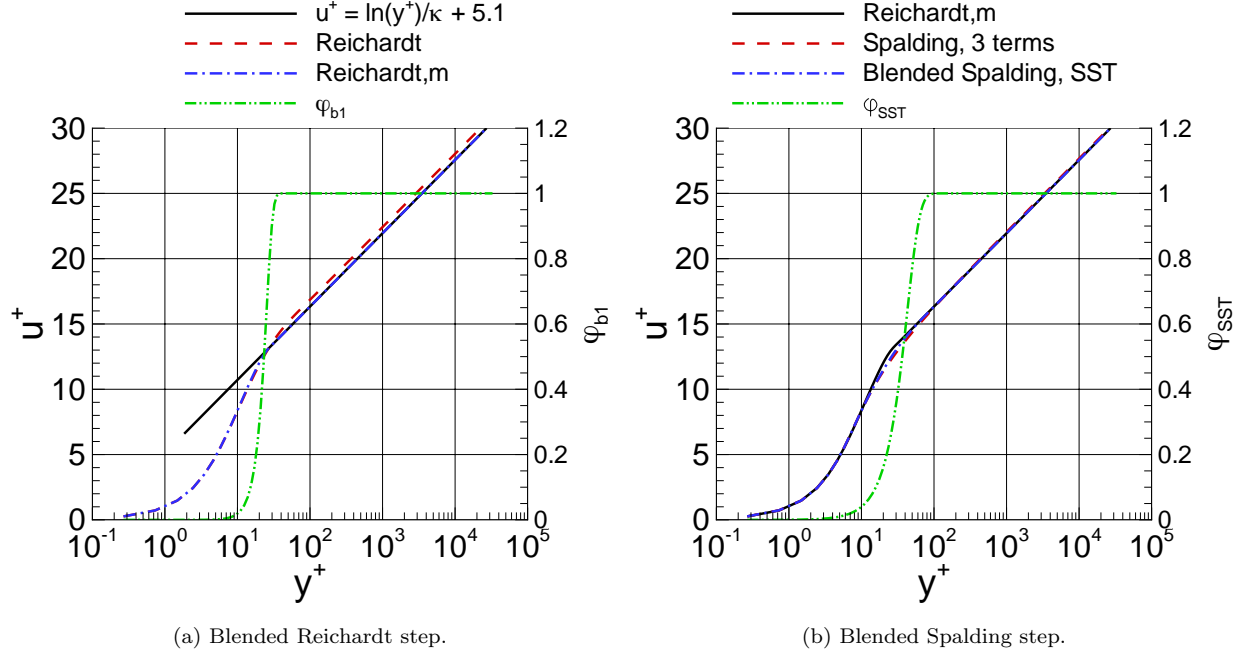


Figure 2: Schematic of blended profiles.

$$u_\tau|_{\text{Reichardt,m}} = (1 - \varphi_{b1}) u_\tau|_{\text{Reichardt}} + \varphi_{b1} u_\tau|_{\text{Log}}, \quad \varphi_{b1} = \tanh(\arg^4), \quad \arg = \frac{y_1^+}{27} \quad (21)$$

In the following step, the friction velocity from Eq. 21 and the friction velocity from the transcendental solution of the Spalding friction velocity,¹⁴ Eq. 22 or Eq. 24, are blended using a hyperbolic tangent functions Eq. 23 or Eq. 25. The wall model, as applied to the SA model, uses a 5-term expansion, while as applied to the SST model, a 3-term expansion is used. Also, slightly different functional forms of the blending are used depending on the turbulence model.

For SA:

$$u_\tau|_{\text{Spalding,5}} \Rightarrow y_1^+ = u_1^+ + e^{-\kappa 5.2} \left(e^{\kappa u_1^+} - 1 - \kappa u_1^+ - \frac{(\kappa u_1^+)^2}{2} - \frac{(\kappa u_1^+)^3}{6} - \frac{(\kappa u_1^+)^4}{24} - \frac{(\kappa u_1^+)^5}{120} \right) \quad (22)$$

$$u_\tau|_{\text{SA}} = (1 - \varphi_{\text{SA}}) u_\tau|_{\text{Spalding}} + \varphi_{\text{SA}} u_\tau|_{\text{Reichardt,m}}, \quad \varphi_{\text{SA}} = \tanh(\arg^3), \quad \arg = \frac{y_1^+}{24}. \quad (23)$$

For SST:

$$u_\tau|_{\text{Spalding,3}} \Rightarrow y_1^+ = u_1^+ + e^{-\kappa 5.2} \left(e^{\kappa u_1^+} - 1 - \kappa u_1^+ - \frac{(\kappa u_1^+)^2}{2} - \frac{(\kappa u_1^+)^3}{6} \right) \quad (24)$$

$$u_\tau|_{\text{SST}} = (1 - \varphi_{\text{SST}}) u_\tau|_{\text{Spalding,3}} + \varphi_{\text{SST}} u_\tau|_{\text{Reichardt,m}}, \quad \varphi_{\text{SST}} = \tanh(\arg^2), \quad \arg = \frac{y_1^+}{50}. \quad (25)$$

The boundary condition for ω , Eqn. 34 in Knopp,⁶ is computed as

$$\omega_{bc} = \varphi_\omega \omega_{b1} + (1 - \varphi_\omega) \omega_{b2}, \quad \varphi_\omega = \tanh(\arg^4), \quad \arg = \frac{y_1^+}{10}, \quad (26)$$

$$\omega_{b1} = \omega_{\text{visc}} + \omega_{\text{log}}, \quad \omega_{b2} = (\omega_{\text{visc}}^{1.2} + \omega_{\text{log}}^{1.2})^{1/1.2}, \quad \omega_{\text{visc}} = \frac{6\nu_1}{\beta_1 y_1^2}, \quad \omega_{\text{log}} = \frac{u_\tau}{\sqrt{\beta^* \kappa y_1}}. \quad (27)$$

D. Compressibility

The effects of compressibility are modeled via a correction to the wall tangential velocity, u_1 , by using van Driest II transformation,¹⁵

$$u_1^* = \frac{1}{a} \left[\sin^{-1} \left(\frac{2a^2 u_1 - b}{\sqrt{b^2 + 4a^2}} \right) + \sin^{-1} \left(\frac{b}{\sqrt{b^2 + 4a^2}} \right) \right], \quad a^2 = \frac{\text{Pr}_t}{c_p T_1}, \quad b^2 = -\frac{\text{Pr}_t}{c_p T_1} \left(\frac{q}{\tau} \right)_{\text{wall}} \quad (28)$$

where u_1^* is used in place of u_1 in any transcendental equation involving the solution of the friction velocity at the wall.

III. Computational Method and Implementation

A. FUN3D Code

FUN3D is an unstructured three-dimensional, implicit, Navier-Stokes code. Roe's flux difference splitting¹⁶ is used for the calculation of the inviscid terms. Other available flux construction methods include HLLC,¹⁷ AUFS,¹⁸ and LDFSS.¹⁹ The default method for calculation of the Jacobian is the flux function of van Leer,²⁰ but the method by Roe and the HLLC, AUFS and LDFSS methods are also available. The use of flux limiters are grid and flow dependent. Flux limiting options include MinMod²¹ and methods by Barth and Jespersen²² and Venkatakrishnan.²³ Other details regarding FUN3D can be found in Anderson and Bonhaus²⁴ and Anderson et al.,²⁵ as well as in the extensive bibliography that is accessible at the FUN3D Web site.²⁶

B. Boundary Element Discretization

Discretization of the computational volume consists of any combination of 4 basic polyhedra: tetrahedral, hexahedral, prismatic, or pyramidal elements. The faces of the volume elements are either triangles or quadrilaterals. The boundaries, therefore, consist only of triangular or quadrilateral faces or combinations of both types of face elements. Each of these faces are divided in to three or four sub-elements, or duals, depending upon being triangular or quadrilateral, respectively.

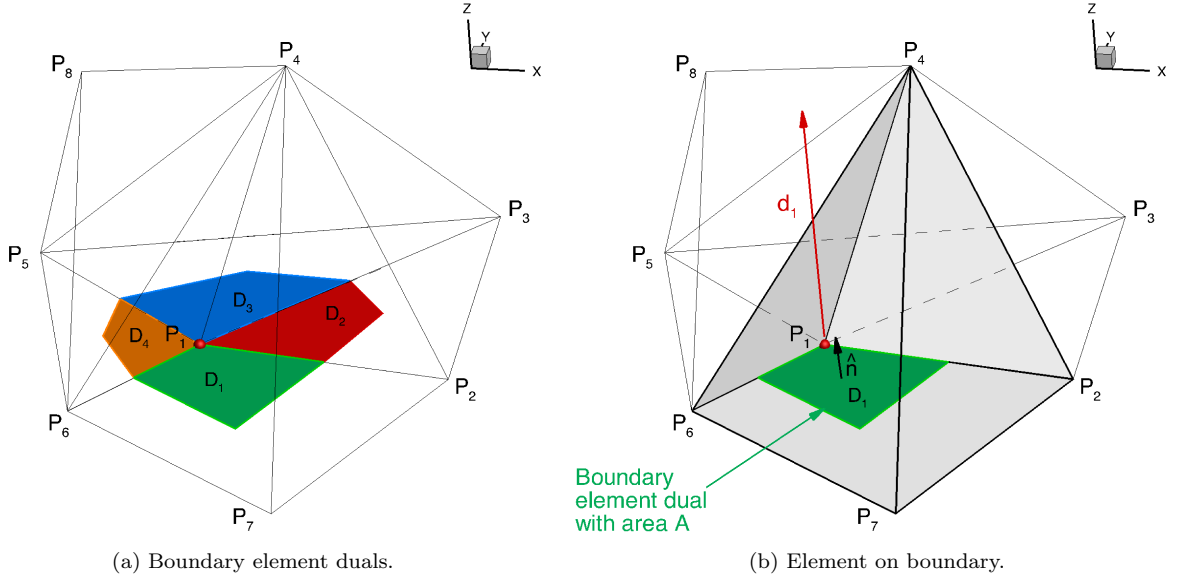


Figure 3: Schematic of a wall boundary element configuration.

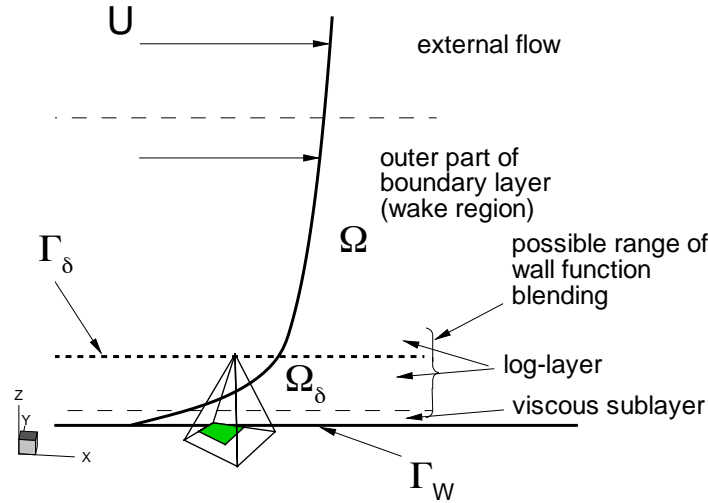


Figure 4: Schematic of domain decomposition (Figure adapted by author from⁶ with permission).

Each node on a boundary face is associated with a number of quadrilaterally shaped sub-elements, or duals. For example, four boundary duals, D_1 through D_4 , associated with the node P_1 , are sketched in Figure 3(a), where P_1, P_2, P_3, P_5, P_6 , and P_7 are all boundary nodes.

Figure 3(b) depicts a pyramidal element with one face associated with the boundary. Several other neighboring tetrahedra are sketched in with lighter weight lines. The heavier black lines, defined by P_1, P_2, P_4, P_6 , and P_7 , are the edges of the example pyramid. P_1, P_2, P_6 , and P_7 are the boundary nodes of the example pyramid. (A shorthand description for this collection of nodes will be [1,2,6,7].)

Four boundary elements have an edge associated with P_1 , one quadrilateral (quad) [1,2,6,7], and three triangles (tri) [1,5,6], [1,3,5] and [1,2,3]. The green quad, D_1 , is one of the previously mentioned duals on the boundary face of the quad and would be used as part of the construction of the flux due to the wall function model. The vector, d_1 , represents the minimum spacing value associated with the boundary node P_1 . The minimum spacing is the average distance of all the off-boundary nodes of the element. In this example with the pyramid, it is the distance off the wall of the point P_4 .

The sample pyramidal element could occupy almost any region of a wall-bounded flow, schematically shown in Fig. 4, depending upon conditions and geometry. In this example, the element extends from the wall, Γ_w , to some point in the log-layer, Γ_δ . The region below Γ_δ is modeled by the wall function and the outer region, Ω , is resolved by the general flow equations. Wall function blending allows accommodation of grid spacing spanning from the viscous sub-layer to approximately 250 wall units above the solid boundary.

Depending upon the type, boundary conditions in FUN3D are applied at either the boundary nodes, e.g., P_1 , or across the boundary element duals, e.g., D_1 . Strong boundary conditions, such as the viscous no-slip wall boundary, in FUN3D nomenclature the `viscous_solid` boundary, explicitly set the velocity at all the boundary nodes, P_1 , to zero. The values of the turbulence model variables, $\tilde{\nu}$, k , and ω are also explicitly set at the wall boundary nodes. A weak boundary condition, such as the viscous no-slip wall boundary and the wall function boundary, `viscous_weak_wall` and `viscous_wall_function` in FUN3D nomenclature, respectively, is applied implicitly at D_1 . The viscous stresses and pressure fluxes are determined for all the boundary duals and added to the right hand side of each of the respective momentum equations. Additionally, to enforce a no-slip velocity condition, a zero momentum flux is assumed across the boundary element.

C. Wall Function Implementation

The wall function and the weak wall boundary condition influence the flow through the stress and pressure terms in the momentum equations. The pressure term is computed and applied in the same way between the two boundary types. With a wall function, the shear stress is modeled using a number of transcendental equations. The weak wall boundary condition, by comparison, computes a shear stress term directly from the flowfield solution and grid element geometry. This section describes the wall function boundary condition.

Solution process

- (1) For each element attached to a wall function boundary, an averaged density, velocity, pressure and viscosity is computed. Just as the minimum spacing value is determined by the average distance of all the off-boundary nodes in the element, the primitive flow variable values are the average of all the off-boundary values and are also designated by the subscript “1”.

$$\vec{q}_1 = \frac{1}{\text{nodes}_{\text{off}}} \sum_{n=1}^{\text{nodes}_{\text{off}}} \vec{q}, \quad \vec{q} = [\rho, u, v, w, p]^T \quad (29)$$

- (2) The off-wall velocities determine the local flow direction from which a tangential velocity is computed.

$$\vec{u}_{\parallel} = \vec{u}_1 - u_{\perp} \hat{n}, \quad u_{\perp} = \vec{u}_1 \cdot \hat{n}, \quad \vec{u}_1 = [u, v, w] \Big|_1 \quad (30)$$

The unit direction of the flow tangential to the wall is then

$$\hat{u}_{\parallel} = \frac{\vec{u}_{\parallel}}{|\vec{u}_{\parallel}|}. \quad (31)$$

- (3) The temperature and density are adjusted according to the magnitude of the tangential velocity,

$$\rho = \bar{\rho} \frac{\bar{T}}{T}, \quad T = \bar{T} - \frac{1}{2}(\gamma - 1) \text{Pr}_t |\vec{u}_{\parallel}|^2, \quad \bar{T} = \gamma \frac{p_1}{\rho_1} \quad (32)$$

and Sutherland’s law is used to determine the dynamic viscosity.

$$\bar{\nu} = \frac{1}{\rho} \left[\frac{(1 + C^*)}{(T + C^*)} T^{3/2} \right], \quad C^* = 110.3/T_{\text{ref}}, \quad T_{\text{ref}} = 288.15\text{K}. \quad (33)$$

- (4) The friction velocity, u_{τ} , is computed solving Eqs. 19, 20 and 21 simultaneously via Newton’s method.
- (5) If the distance from the boundary in wall units, $y_1^+ = (u_{\tau} d_1 / \bar{\nu})$, is less than 250, Newton’s method is again used, this time to solve Spalding’s relationship, Eq. 22, along with blending equation, Eq. 23, when using the SA turbulence model. Eqs. 24 and 25 are used for the SST turbulence model.

If the distance from the boundary is greater than 250, Spalding’s relationship becomes ill-conditioned and difficult to solve. In that case, step (5) is not executed, and the friction velocity from step (4) is used.

- (6) The shear stress on the boundary is

$$\tau_{\text{wf}} = \rho u_{\tau}^2|_{\text{wf}} \quad (34)$$

- (7) The shear stress, τ_{wf} , computed from the wall function, the pressure, p , and the area of the element dual on the wall, A , are used to compute the momentum flux contribution. Heat transfer is not accounted for in the current formulation.

$$\mathcal{F}|_{D_1} = \tau_{\text{wf}} \hat{u}_{\parallel} A - p \hat{n} A \quad (35)$$

IV. Test Cases

The four geometries used to validate the implementation of the wall function models are described in sub-sections A through D. Table 1 lists relevant aspects of the simulation for each case. The flat plate and asymmetric diffuser flows are low speed with little, if any, compressibility effects. The asymmetric diffuser flow has both flow separation and re-attachment points. The flow about the RAE 2282 airfoil is attached for the specific flow conditions chosen for this report, and the flow about the ONERA M6 wing is a 3-D problem with flow separation. Comparisons are made with historic, canonical data or experimental results where available.

Table 1: Test geometry setup.

Geometry	Grid	Flow physics
Flat plate	2D	incompressible, $dp/dx \approx 0$, attached flow
Asymmetric subsonic diffuser	2D	incompressible, separated flow
RAE 2822 airfoil	2D	compressible, attached flow
ONERA M6 wing	3D	compressible, separated flow

A. Zero pressure gradient flat plate

In this section, the initial validation tests of the wall function model are discussed. Friction velocity, local skin friction and mean flow profiles are compared with results from a wall integration turbulence model for the flat plate and are shown in Figs. 7, 8, and 9, respectively. The determination of the friction velocity was explored using three approaches for specifying grid spacing and grid density:

1. Uniform refinement
2. Variable wall spacing with fixed grid dimensions, log-layer unpacked (LLU)
3. Viscous layer node removal from a baseline grid, log-layer packed (LLP)

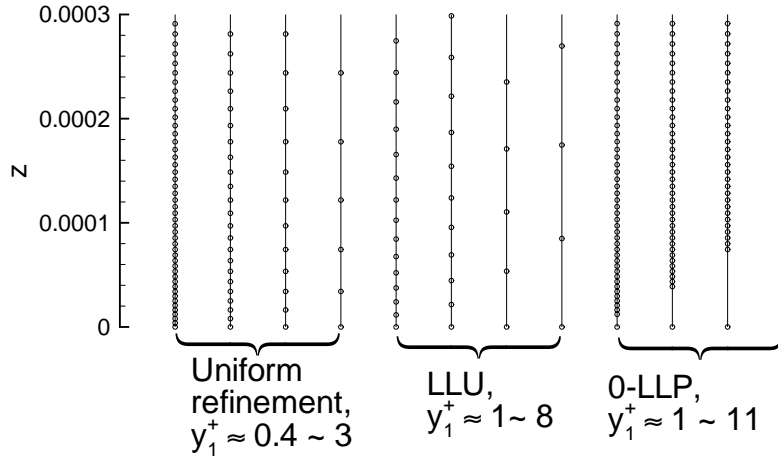


Figure 5: Comparison of near-wall node spacing approaches.

A sample of node distributions for these approaches are sketched in Fig. 5. The generation of uniformly refined grids is used for assessing grid convergence order properties, see the first four lines on the left. Producing wall function grids through successive coarsening of a very fine baseline, though, can inadvertently reduce the resolution in other regions of the flow. Simply increasing the wall spacing, referred to as log-layer unpacked²⁷ (LLU) spacing, can produce grids with the same issues as successive coarsening. These grids, though, are

often more convenient to generate. The middle four lines in the figure are examples of LLU node spacing. Counting from the left, the fourth and the seventh lines appear to have quite similar distributions. Node removed grids, or LLP spacing, maintain resolution away from the wall, as shown with the last four lines on the right side of the figure, while providing a large initial wall distance. The particular LLP examples shown use the finest uniform refinement grid as the starting point and successively remove a number of nodes between the wall and the outer region.

Table 2: Grid parameters for the flat plate.

Level	Dimensions (baseline)	Nodes (baseline)	Nodes removed	Spacing range [m]	y_1^+ range
0	897 x 449	402753	-	4.0×10^{-6}	0.4
1	449 x 225	101025	-	8.0×10^{-6}	0.8
2	225 x 113	25425	-	1.6×10^{-5}	1.5
3	113 x 57	6441	-	3.4×10^{-5}	3.2
LLU	257 x 129	33153	-	$1.16 \times 10^{-5} \sim 1.05 \times 10^{-3}$	1. \sim 98.
0-LLP	897 x 449	402753	0 \sim 40	$4.0 \times 10^{-6} \sim 8.4 \times 10^{-4}$	0.4 \sim 23.
1-LLP	449 x 225	101025	0 \sim 40	$8.0 \times 10^{-6} \sim 8.4 \times 10^{-4}$	0.8 \sim 76.

The parameters for each of the gridding approaches are listed in Table 2. The wall spacing of the uniform refinement series spanned from roughly one-half to 3 wall units. Each level removes every other node in the streamwise and normal directions. Level 0 is the finest grid. With every 8 nodes removed, Level 3 is the most coarse grid. The LLU approach fixed both the streamwise and vertical number of nodes in the grid and only increased the initial wall spacing, and then continued expanding away the wall. As mentioned previously, grid density near the wall is reduced with this method, possibly compromising resolution of flow features in the region. The baseline grid for the LLU series was between the spacing of the level 1 and 2 uniform refinement series. A total of 13 grids were generated for the LLU series with the parameters listed in Table 2.

A total of 11 grids were generated for the each of the two log-layer packed (LLP) series. Between 0 and 40 layers of nodes were removed from two of the uniform refinement grids. This method, therefore, retained the same distribution of nodes in the region above the wall function space. The 0-LLP series, using the level 0 uniform refinement grid as the baseline, spanned the wall spacing range from 0.4 to 23, depending upon the number of layers removed. The 1-LLP series, using the level 1 uniform refinement grid as the baseline, spanned the wall spacing range from 0.8 to 76, again, depending upon the number of layers removed. The grid parameters are listed in Table 2. All of the grids consisted of hexahedral elements and were one-cell wide.

The 1-equation turbulence model of Spalart-Allmaras^{7,8} and the 2-equation turbulence model of Menter⁹ were used. The simulation conditions were $M_\infty = 0.097$ and $Re_L = 2.7 \times 10^6$, ($L = 1$ m). All solutions were run second-order spatially accurate and in 2-dimensional mode. Solutions were obtained on the uniformly refined grids using both the wall integration and wall function models. Only wall function solutions were obtained on the LLU and LLP grids.

Iterative convergence was obtained for all solutions with the grids listed in Table 2. Each solution residual history is not shown here, but the set of continuity equation residual histories shown in Fig. 6 are representative of the convergence obtains for all the solutions obtained in this section. The Spalart-Allmaras turbulence model converged within, 1000 or so iterations, while on the order of 10,000 iterations were required to obtain a similar level of convergence using the SST turbulence model. With model validation being the primary intent of this study, more effort was extended towards obtaining iterative convergence than finding an optimal solution path.

The first test examines the convergence of the predicted friction velocity with grid size. When applied to the uniformly refined grids, the wall function predicted the same friction velocity as the wall integration models, as shown by a comparison of the circle and square symbols in Fig. 7, regardless of turbulence model. Identical convergence, for this sequence of grids, indicates that solutions can be obtained on wall integration grids with wall functions.

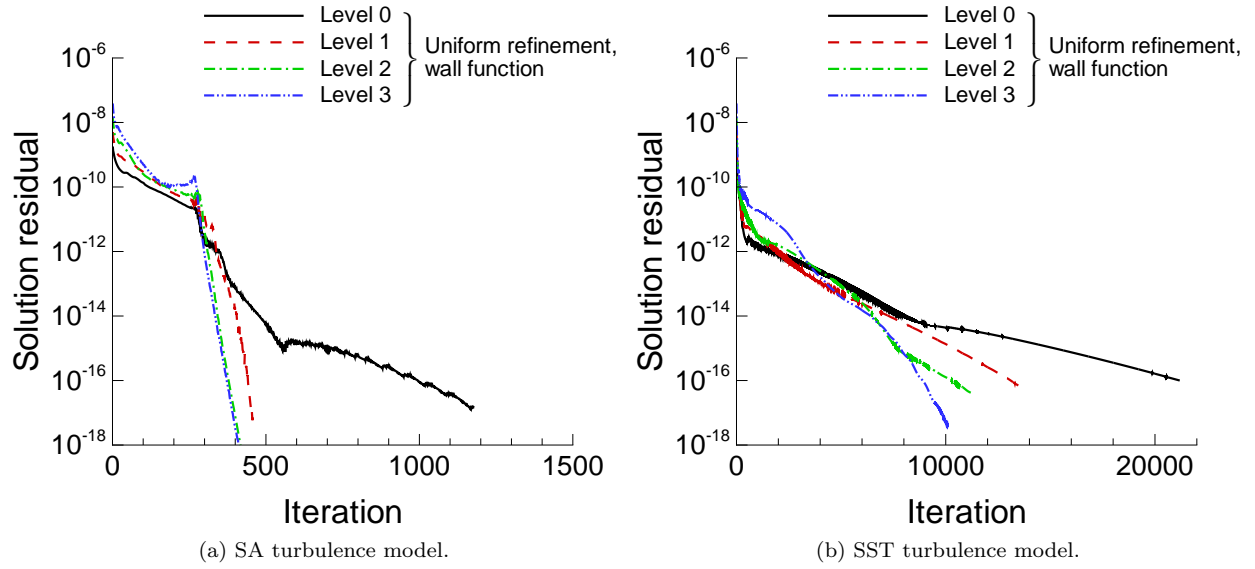


Figure 6: Solution residual, continuity equation, flat plate, $M_\infty = 0.097$, $Re_L = 2.7 \times 10^6$

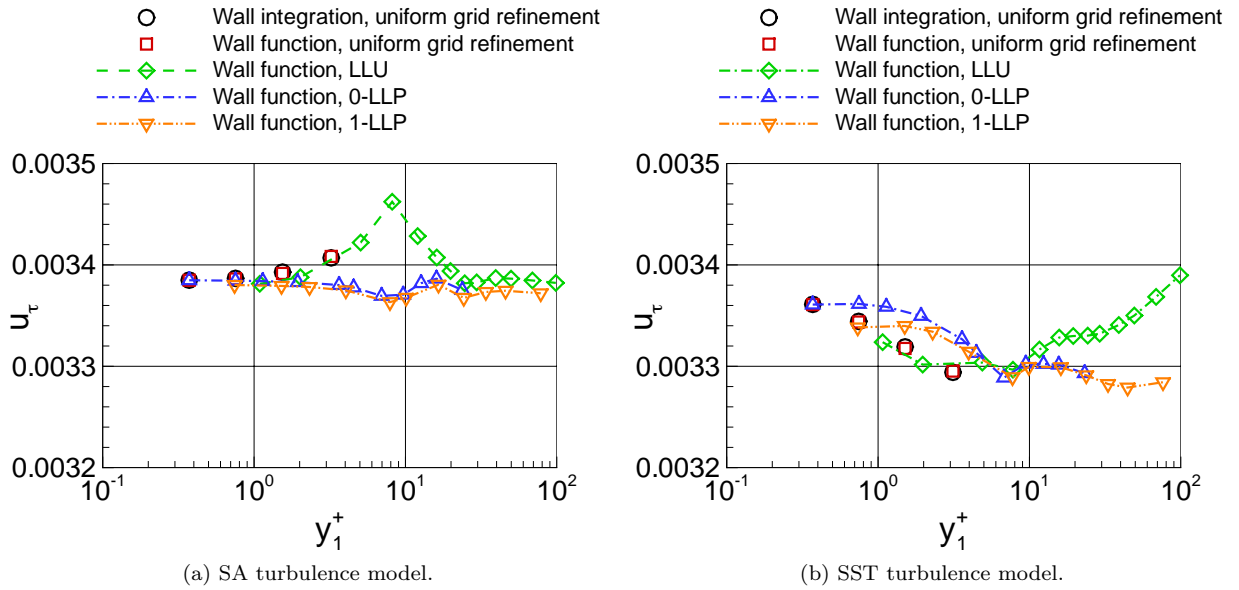


Figure 7: Comparison of predicted friction velocity, $x = 4.0m$, $M_\infty = 0.097$, $Re_x = 1.1 \times 10^7$

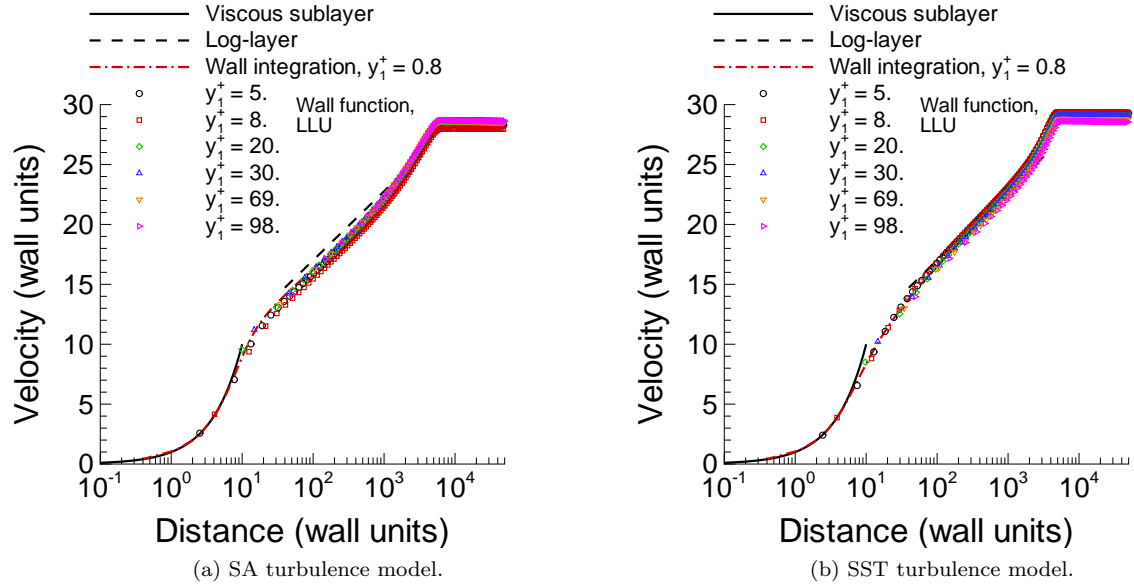


Figure 8: Comparison of predicted mean flow profiles, $x = 4.0\text{m}$, $M_\infty = 0.097$, $Re_x = 1.1 \times 10^7$

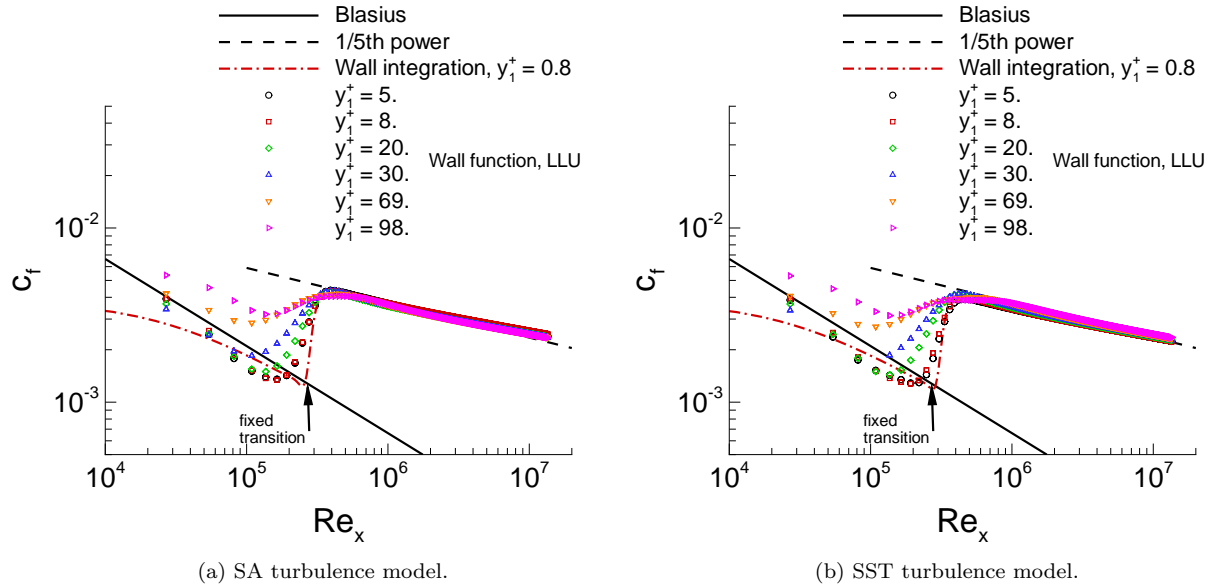


Figure 9: Comparison of predicted local skin friction, $M_\infty = 0.097$, $Re_L = 2.7 \times 10^6$

The first three grids for the LLU series, in the range $1 \lesssim y_1^+ \lesssim 3$, aligned closely with the uniform refinement grids. The larger initial wall spacing results diverged in the region of the buffer for the SA results, and generally above the buffer region for the SST results. Results obtained on LLU grids were inconsistent at best.

Nearly constant friction velocities were predicted by solutions obtained on the series of LLP grids using the SA based wall function. Solutions based on the SST wall function were less constant across the viscous sub-layer, compared to the SA solutions. The predicted friction velocity did finally level out when the initial spacing was above $y_1^+ = 8$. The SST model varied as much as 2%, from the finest to the coarsest, and was more consistent than the results using the LLU grids; as shown by a comparison of the diamond to the delta and triangle symbols in Fig. 7.

Computed wall integration and wall function mean flow velocity profiles using the LLU grid are plotted in wall units and compared with empirical data in Fig. 8. The wall integration solution is from the level 1 refined grid. Though the calculations using the LLU grid show a relatively wide variation in the predicted friction velocity, the mean flow velocity profiles were very close to the wall integration profile. The calculations using the other uniform refinement and LLP grids are not plotted but were similar to these results.

Computed wall integration and wall function local skin friction distributions using the LLU grid are plotted with empirical data in Fig. 9. Similar to the mean flow profiles plotted previously, the wall integration solution is from the level 1 refined grid. Downstream of the fixed transition, the LLU local skin friction closely matched the wall integration values. The calculations using the other uniform refinement and LLP grids are not plotted but were similar to these results.

B. Asymmetric subsonic diffuser

The second test case was the asymmetric diffuser of Buice and Eaton.²⁸ The adverse pressure gradient due to the diffuser is sufficient to cause the flow to separate. The flow subsequently re-attaches downstream of the diffuser in the constant area outflow section. Experimental mean flow and shear stress profiles, as well as surface static pressure and local skin friction data, are compared with solutions obtained with both wall integration and wall function models.

The reference Mach number was set at 0.06. The Reynolds number per reference length was 20,000, where the reference length was the upstream channel height, H . The diffuser section was $77 H$ long, preceded by a $110 H$ long channel. The wall integration grid was a single-block, single-cell wide, hexahedral type grid. Two wall function, LLP, grids were created by removing the first 10 and first 20 wall layers, respectively, from the baseline wall integration grid. Layers were removed from both the upper and lower walls. Figure 10 is a sketch of the diffuser geometry, along with detail views of the start and end of the diffuser section for the 20 node removed grid.

Iterative convergence was obtained for all solutions. Continuity equation residuals are shown in Fig. 11 for all the grid and turbulence model variations. With model validation being the primary intent of this study, more effort was put towards obtaining iterative convergence than finding optimal solution paths.

Local wall spacing distributions are shown in Fig. 12, for each of the grids. The average spacing of the upper wall was similar to the lower wall, so for clarity, only the lower wall distributions are plotted in the figure. In the region of the diffuser, $0 < x/H < 20$, the first cell spacing in wall units varied from an average of 1 to 20, depending upon location. The local minima in y_1^+ around $x/H = 4$ and 30 are indicative of the flow separation and re-attachment points. Generally the same distribution of y_1^+ for each grid type occurred, regardless of turbulence and wall function model.

Figure 13 shows the velocity profiles in the diffuser with and without wall functions. For purposes of visualization, the vertical and horizontal axes are scaled differently so that the velocity profiles are shown in the context of the diffuser geometry. The velocity is normalized by the bulk velocity, U_b , at the entrance to the diffuser, $x/H = 0$. Computed turbulent shear stress for each wall model is compared with experimental data in Fig. 14. A similar visualization is used here where the vertical and horizontal axes are scaled differently so that the shear stress profiles are shown in the context of the diffuser geometry. The shear stress is normalized by the square of the bulk velocity, U_b . Generally, the same result was achieved across grid types and turbulence models.

Computed local skin friction on the lower wall of the diffuser, for each wall model, is plotted with experimental data in Fig. 15. Solutions obtained with the SST model separated from the diffuser wall further upstream of the experimental data than solutions obtained using the SA model. It is fortuitous

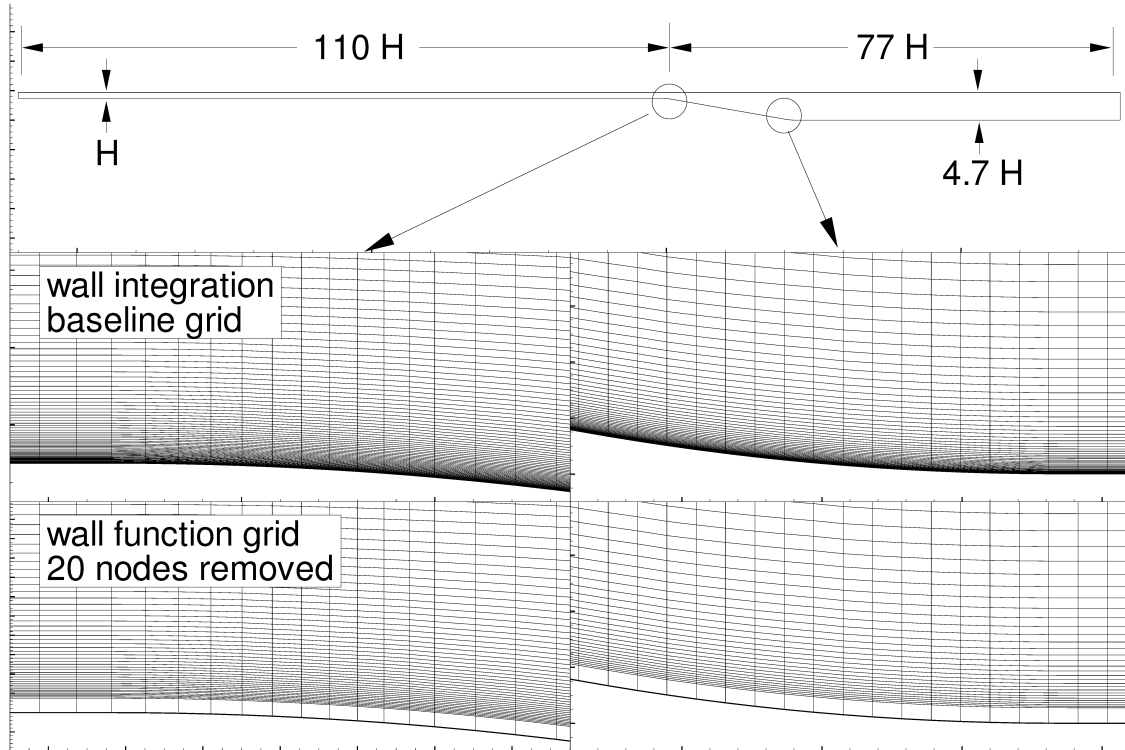


Figure 10: Sketch of asymmetric subsonic diffuser.

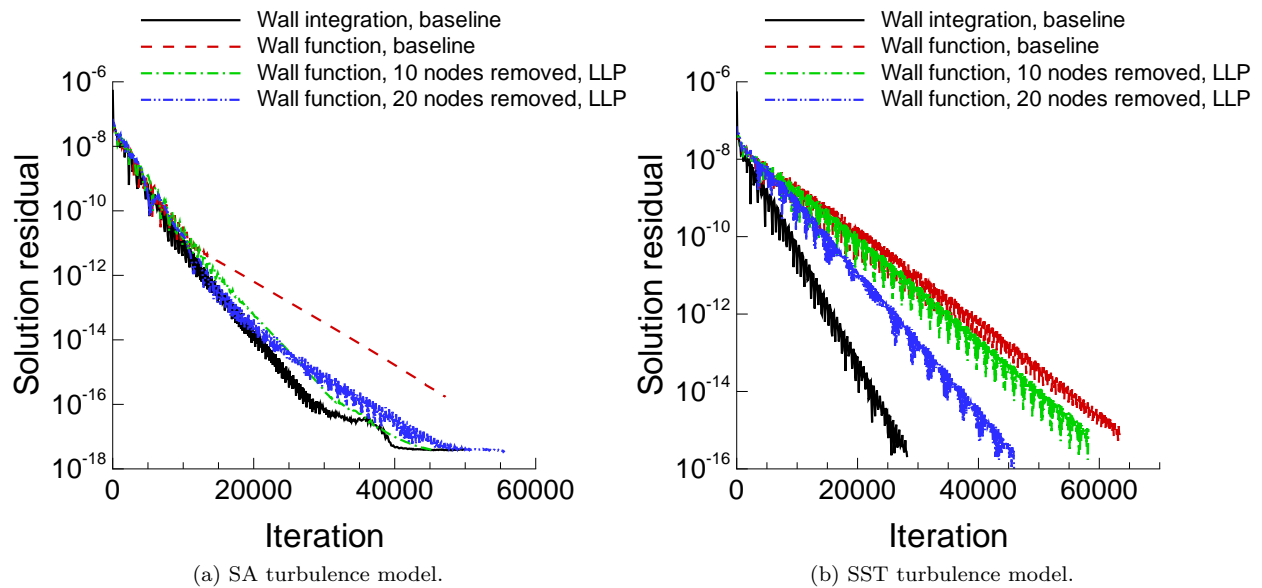


Figure 11: Solution residual, continuity equation, asymmetric diffuser.

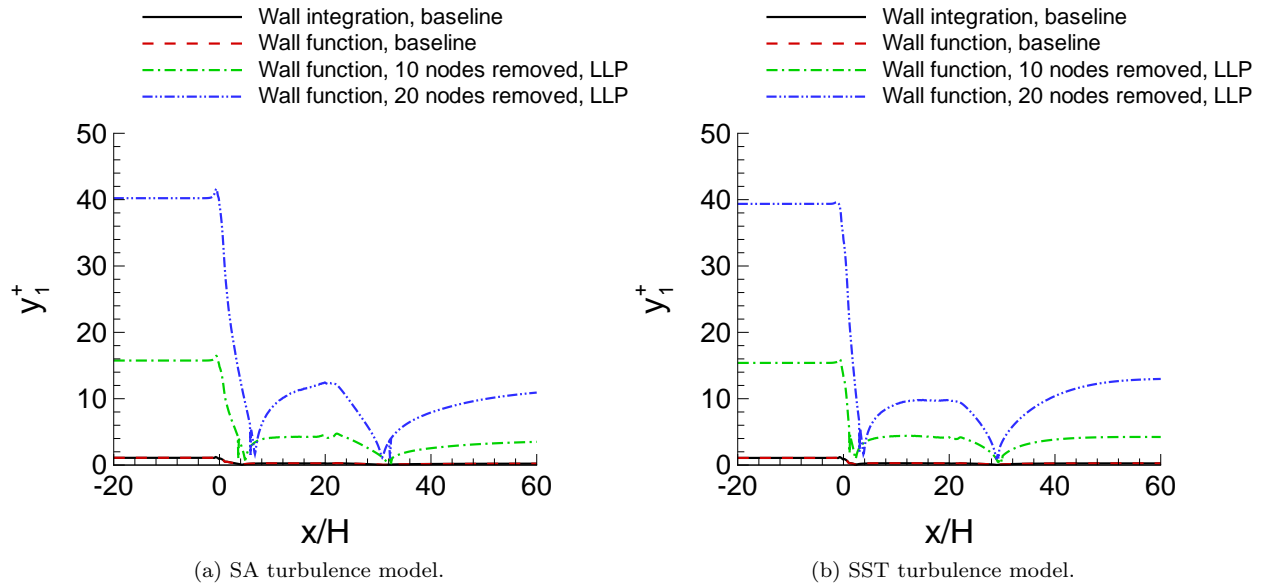


Figure 12: Upper and lower wall spacing distribution, asymmetric subsonic diffuser, $M_\infty = 0.06$, $Re = 20,000$.

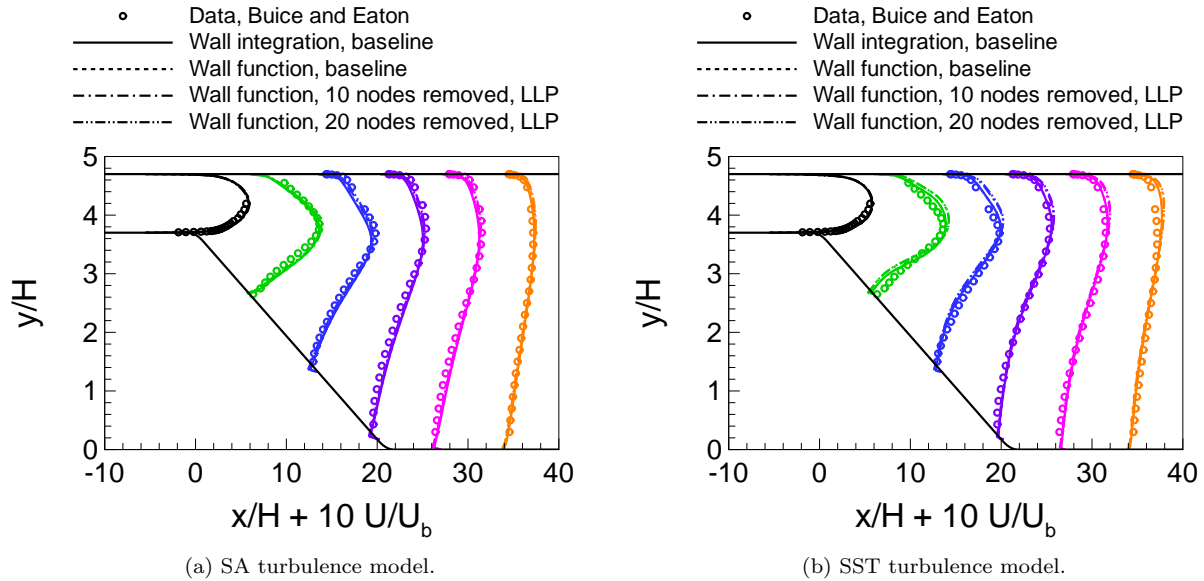


Figure 13: Velocity profiles, asymmetric subsonic diffuser, $M_\infty = 0.06$, $Re = 20,000$.

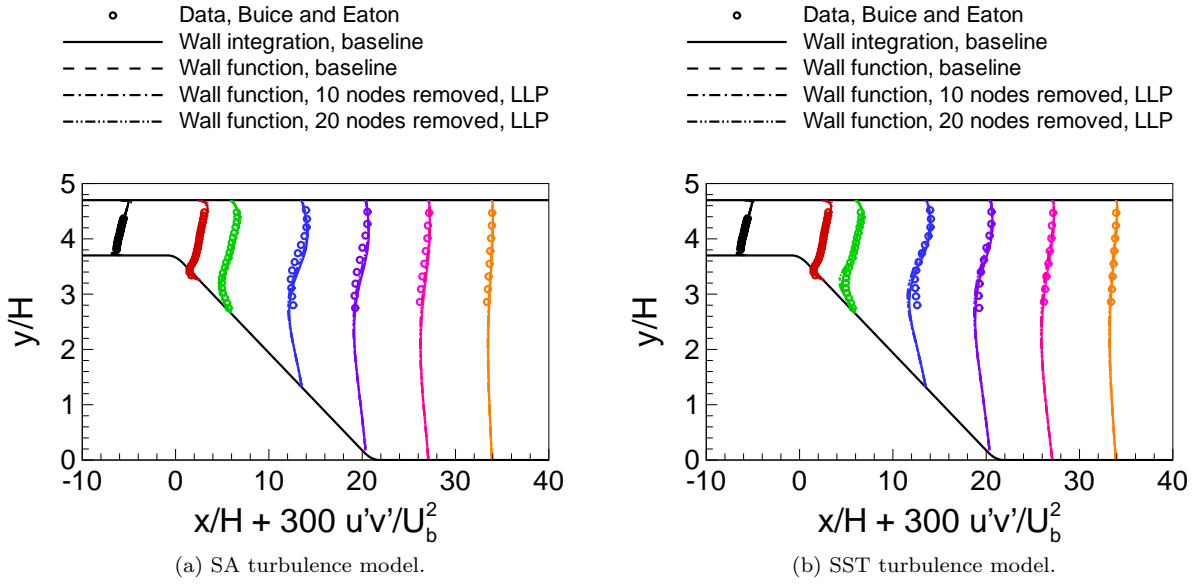


Figure 14: Turbulent shear stress profiles, asymmetric subsonic diffuser, $M_\infty = 0.06$, $Re = 20,000$.

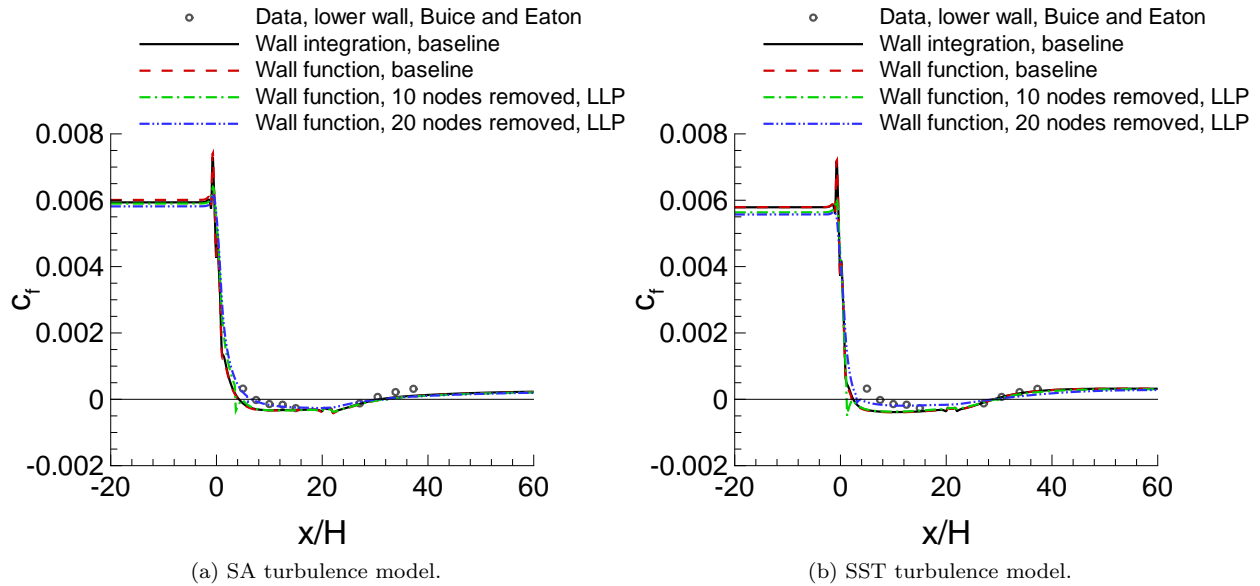


Figure 15: Local skin friction, asymmetric subsonic diffuser, $M_\infty = 0.06$, $Re = 20,000$.

that the point of flow separation computed using the 20 node removed grid is closer to the data than the computation with 10 node removed grid.

C. RAE 2822 airfoil

The third test case is the RAE 2822 airfoil.²⁹ Wall integration and wall function solutions were obtained on a set of structured LLU grids and a separate set of structured LLP grids, which were converted to an unstructured format for use in this study. The first set of solutions were obtained on a sequence of grids with constant node count, with wall spacings ranging from approximately 1 for wall integration calculations to 10, 20 and 40 wall units (on average) for the wall function calculations. The second hexahedral grid came from the NPARC Alliance validation archive.^{30,31} In addition to the baseline grid, 5 layers of nodes were removed from the grid layers adjacent to the airfoil surface. Solutions using the “node removed” grid, denoted again with LLP, are shown along with the initial set of LLU grids.

Distributions of grid, wall spacing (y_1^+), surface pressure coefficients, solution residual and skin friction are shown in Figs. 16 through 20. A hyperbolic grid generator was used to create the first set of C-type grids. All of the grids had 161 grid points normal to the airfoil surface, 513 points on the airfoil and 64 points in the wake region (upper and lower), for a total of 641 points in the tangential direction. For the $y_1^+ \sim 1$ grid, the distance of the first point from the surface is 0.000005 chords. The step size in the tangential direction at the leading edge is 0.0008 and at the trailing edge is 0.0012 chords. The far-field and downstream boundaries were approximately 20 chords away. The geometric progression ratio near the surface was approximately 1.1. The wall function grids were LLU type, so they were created by merely increasing the spacing at the wall, as listed in Table 3. All other grid generation parameters were unchanged. As stated earlier, the second hexahedral grid came from the NPARC Alliance validation archive with the parameters also listed in Table 3.

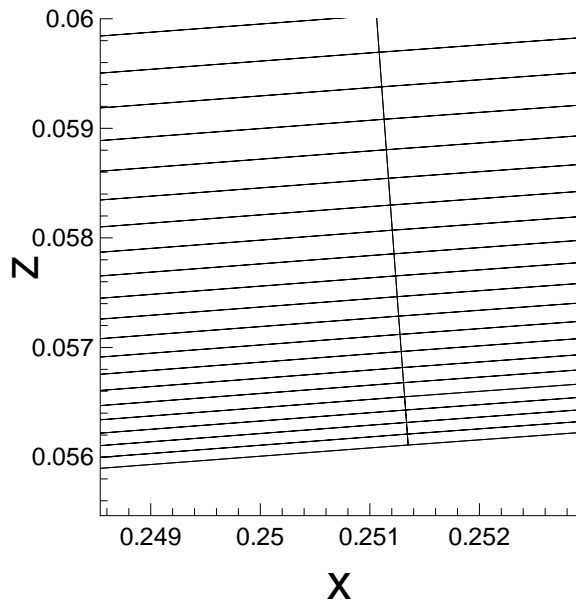
Table 3: Grid parameters, RAE 2822 airfoil.

Grid	Normal spacing [chord]	y_1^+	Dimensions	Nodes
Wall integration	5.0×10^{-6}	1.	641×161	103201
Wall function (LLU)	5.0×10^{-5}	10.	641×161	103201
Wall function (LLU)	1.0×10^{-4}	20.	641×161	103201
Wall function (LLU)	2.0×10^{-4}	40.	641×161	103201
Wall integration (NPARC)	1.2×10^{-5}	2.5	369×65	47904
Wall function (LLP)	1.3×10^{-4}	25.	369×60	44214

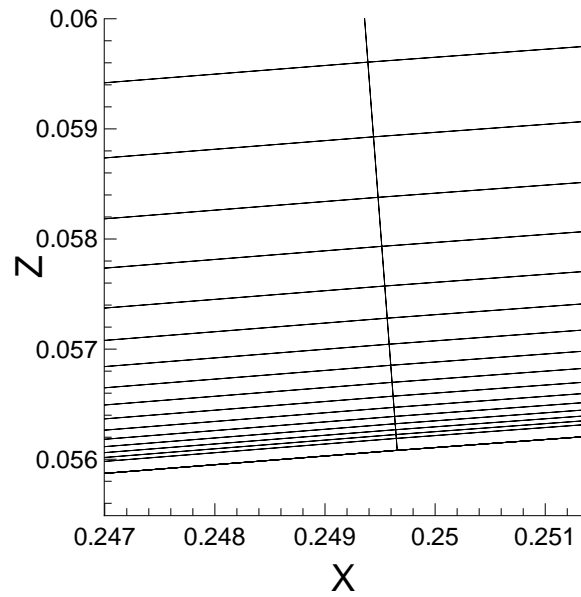
A comparison of the distribution of computational nodes normal to the airfoil around $x/c \sim 0.25$, is shown in Fig. 16. Both grids have roughly the same wall spacing of $y_1^+ \sim 20$ to 25. Whether or not this kind of difference in grid distribution makes a difference is likely quite problem dependent. Iterative convergence was achieved for all grid variations for both the SA and SST turbulence model/wall function combinations run, see Fig. 17.

Wall spacing, (y_1^+), distributions for all of the grids are plotted in Fig. 18. No effort is made to differentiate upper surface values from lower surface values, as the intent of the plot is merely a general evaluation of the wall spacing trend. Exact averages were not calculated, but in general, the wall spacing annotation for each grid is a reasonable representation of the actual spacing of the calculation.

Surface static pressure distributions for all the grid variations are plotted in Fig. 19. No significant differences in the solutions are seen. Upper surface local skin friction distributions for all the grid variations are plotted in Fig. 20. The computed skin friction distributions from the six different grids were very close in level and variation. It is difficult to draw a significant conclusion from these plots alone. The integrated forces and moments for each of the grids are listed in Tables 4 and 5. The solution obtained using the wall function (LLP) grid had the largest deviation, using the wall integration $y_1^+ = 1$ as the basis for comparison, being off by 3% in lift, 2% in drag and 5% in pitching moment. The lift, drag and pitching moment, obtained with the LLP grid, was below the results from the $y_1^+ = 20$ and $y_1^+ = 40$ grids for lift, drag and moment.

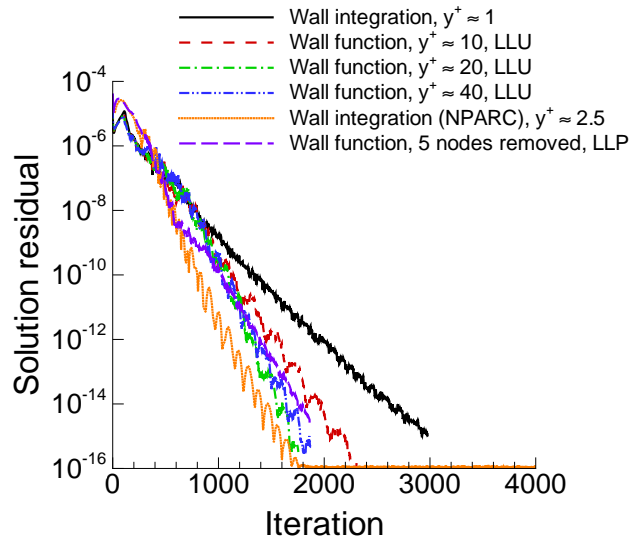


(a) $y_1^+ \sim 20$, LLU.

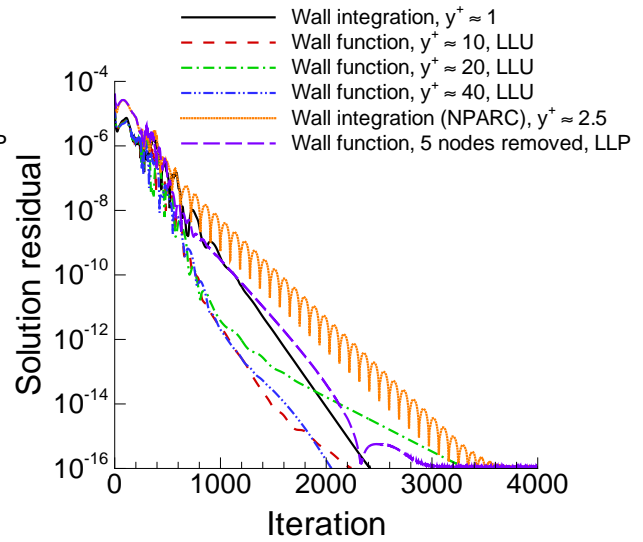


(b) $y_1^+ \sim 25$, LLP.

Figure 16: Detail of grid distribution, RAE 2822, $x/c \sim 0.25$



(a) SA turbulence model.



(b) SST turbulence model.

Figure 17: Solution residual, continuity equation, RAE 2822, Case 9

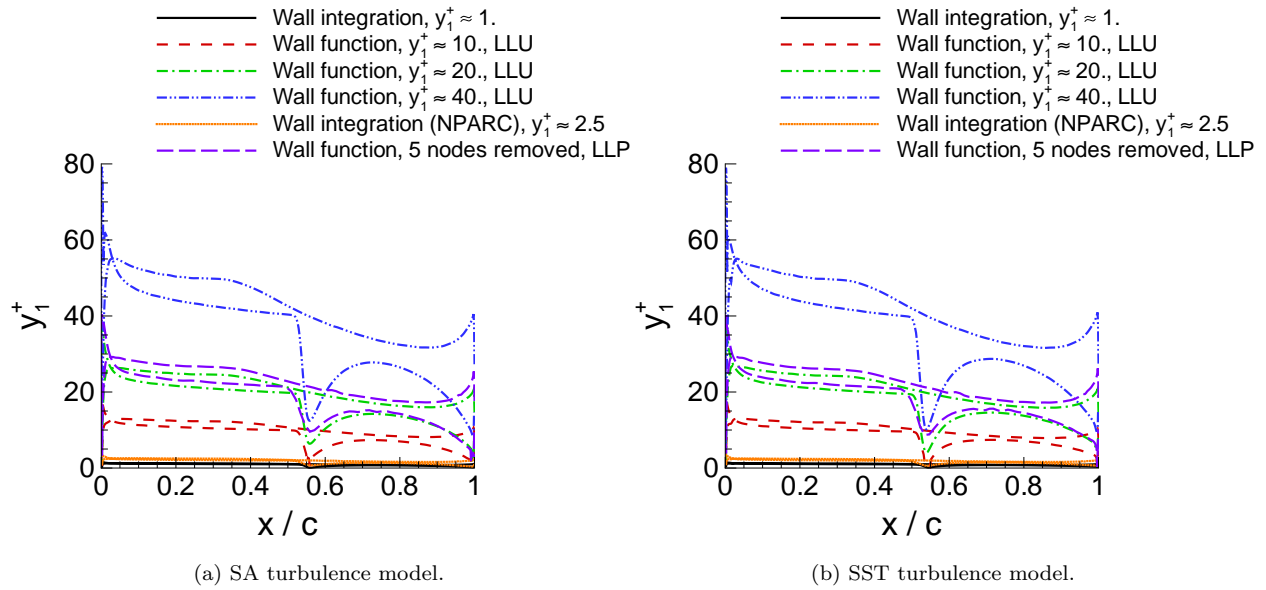


Figure 18: Upper and lower wall spacing distributions, RAE 2822, Case 9

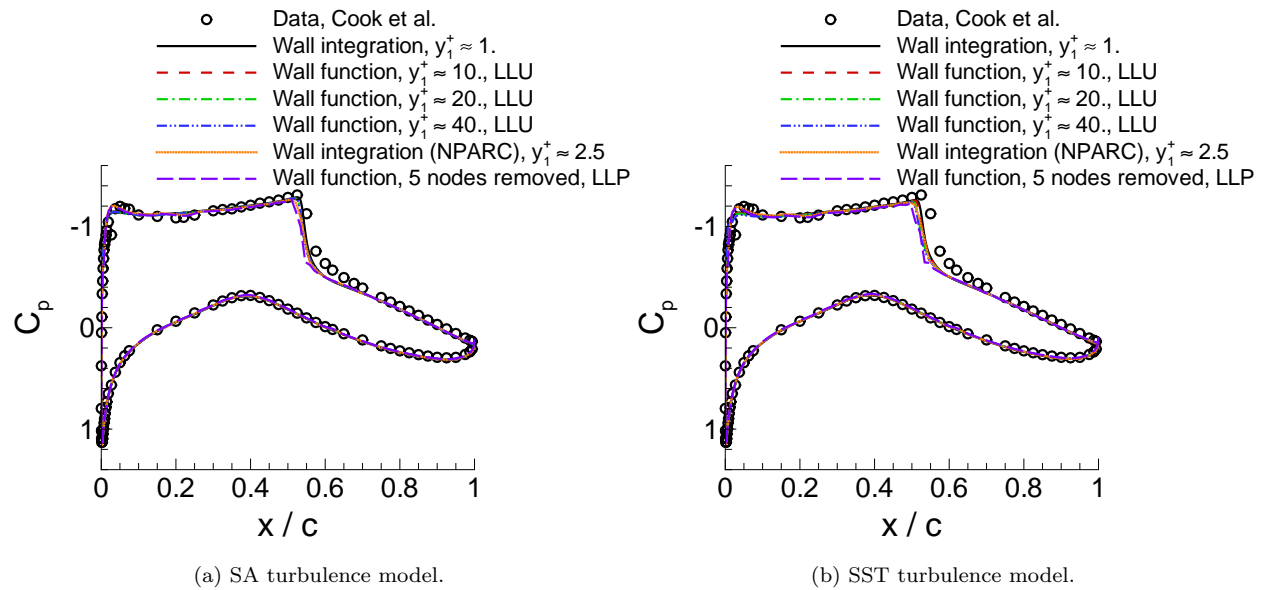


Figure 19: Pressure coefficient distributions, RAE 2822, Case 9

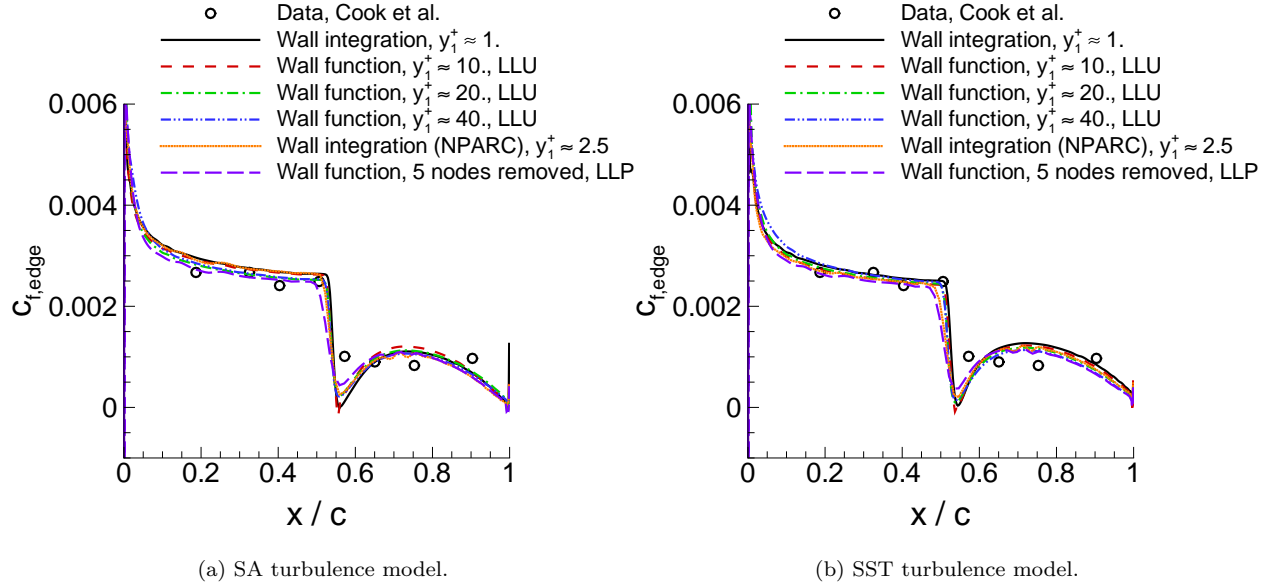


Figure 20: Skin friction coefficient distributions, RAE 2822, Case 9

Table 4: Computed forces and moments, RAE 2822, SA turbulence model.

Grid	y_1^+	Lift			Drag			Pitching moment
		total	pressure	viscous	total	pressure	viscous	
Wall integration	1.	0.791	0.791	0.000	0.0173	0.0117	0.0056	-0.090
Wall function (LLU)	10.	0.781	0.781	0.000	0.0171	0.0114	0.0057	-0.088
Wall function (LLU)	20.	0.782	0.782	0.000	0.0171	0.0115	0.0056	-0.089
Wall function (LLU)	40.	0.781	0.781	0.000	0.0172	0.0116	0.0056	-0.089
Wall integration (NPARC)	2.5	0.784	0.784	0.000	0.0175	0.0118	0.0057	-0.089
Wall function (LLP)	25.	0.769	0.769	0.000	0.0169	0.0114	0.0055	-0.086

Table 5: Computed forces and moments, RAE 2822, SST turbulence model.

Grid	y_1^+	Lift			Drag			Pitching moment
		total	pressure	viscous	total	pressure	viscous	
Wall integration	1.	0.768	0.768	0.000	0.0164	0.0109	0.0055	-0.086
Wall function (LLU)	10.	0.764	0.764	0.000	0.0162	0.0108	0.0054	-0.085
Wall function (LLU)	20.	0.756	0.756	0.000	0.0161	0.0107	0.0054	-0.084
Wall function, (LLU)	40.	0.752	0.752	0.000	0.0162	0.0107	0.0055	-0.083
Wall integration (NPARC)	2.5	0.763	0.763	0.000	0.0163	0.0110	0.0053	-0.084
Wall function (LLP)	25.	0.742	0.742	0.000	0.0159	0.0106	0.0053	-0.080

D. ONERA M6 wing

The fourth configuration is the ONERA M6 wing.³² This geometry is well known and often used in CFD validation studies.^{33–37} The M6 wing is challenging not only for the highly three-dimensional nature of the flow, but the upper surface shock and degree of flow separation. These features are quite prominent even at 3 and 4 degrees angle of attack.

The unstructured grids for the M6 were generated with the VGRID v4.0 advancing-layer and advancing-front grid generation software package.³⁸ VGRID has two types of spacing requirements: the “inviscid” spacing distributions are used in the advancing-front region of the grid, and the “viscous” spacing distributions are used near the solid body in the advancing-layer regions of the grid where high stretching is required. The clustering of points normal to the surface was computed according to the VGRID stretching function,³⁸ $\delta_n = \delta_1[1 + r_1(1 + r_2)^{n-1}]^{n-1}$, where δ_n is the normal spacing of the n^{th} layer, δ_1 is the spacing of the first layer, and the factors r_1 and r_2 are constants that determine the rate of stretching. (Note if r_2 is zero the stretching is geometric.)

Table 6: Grid parameters for the ONERA M6 wing.

	Level	Nodes	r_1	r_2	y_1^+
Wall integration		6.6×10^6	0.15	0.02	~ 1 .
Wall function, LLU		6.1×10^6	0.10	0.02	~ 25 .
Wall function, LLU		5.7×10^6	0.10	0.02	~ 50 .

Three different grids were generated for this study: a wall integration grid with a nominal y_1^+ of 1, and two LLU wall function grids with nominal y_1^+ of 25 and 50, and are listed in Table 6. All of the grids use the same set of inviscid spacing distributions, and therefore, the surface grid for each grid has essentially the same surface spacing distributions. For the integration to the wall grid, the grid normal spacing is set such that an average normalized coordinate y^+ is less than one for the first grid cell at the wall for the majority of the wing. The advancing-layer stretching rates, r_1 and r_2 , are 0.15 and 0.02, respectively. The total number of grid nodes is 6.6 million. For the second grid, the grid normal spacing is increased to 25, and the advancing-layer stretching rates, r_1 and r_2 , are 0.10 and 0.02, respectively. The total number of grid nodes for the second grid is 6.1 million. For the third grid, the grid normal spacing is increased to 50, and the advancing-layer stretching rates, r_1 and r_2 , are 0.10 and 0.02, respectively. The total number of grid nodes is 5.7 million.

The grids for the isolated wing extend approximately 33 MAC away from the surface to a square outer boundary with a symmetry condition on the centerline. The maximum spacing at the wing grid outer boundary is approximately 0.05 MAC. The characteristic chordwise spacing at the leading edge is approximately 0.001 MAC. The characteristic chordwise spacing at the trailing edge is approximately 0.002 MAC. There is no spanwise grid stretching at the leading or trailing edge. The characteristic spanwise spacings at the root and tip are approximately 0.01 and 0.004 MAC, respectively. A cylindrical volume of refinement is set around the wing surface such that within this volume the maximum grid spacing cannot exceed 0.02 MAC near the root and 0.005 MAC at the tip. This cylindrical volume of refinement was achieved by utilizing VGRID volume sources.³⁹ The total number of wing surface points is approximately 107,000 for each of the grids.

A comparison of the relative density of the wall integration grid and the LLU $y_1^+ \sim 50$ grid is shown in Fig. 21. As expected, the near-wall grid density is significantly reduced with the larger wall spacing.

The M6 wing was run at a Reynolds number of 14.0 million/chord (21.7 million/meter), freestream Mach number of 0.84, a freestream temperature of 540.0K, and at 3.06 and 4.08 degrees angle of attack. Solution residuals for the continuity equation are plotted in Fig. 22. Only six orders of magnitude reduction in continuity equation residual for the SA calculations at $\alpha = 3.06^\circ$ was achieved. Eight orders of magnitude reduction, or better, in the continuity equation was achieved with the SST model calculations, as well as, the $\alpha = 4.08^\circ$ calculations. The Venkat limiter²³ was required for the $\alpha = 4.08^\circ$ calculations. The limiter was frozen after the first 4000 iterations, which improved the residual convergence after that point.

Figure 23 is representative of the difference between the various simulations and experimental data. Very good agreement of pressure coefficient distributions was obtained between wall integration and the two wall function grid solutions at $\alpha = 3.06^\circ$ degrees, though neither the wall integration nor the wall function

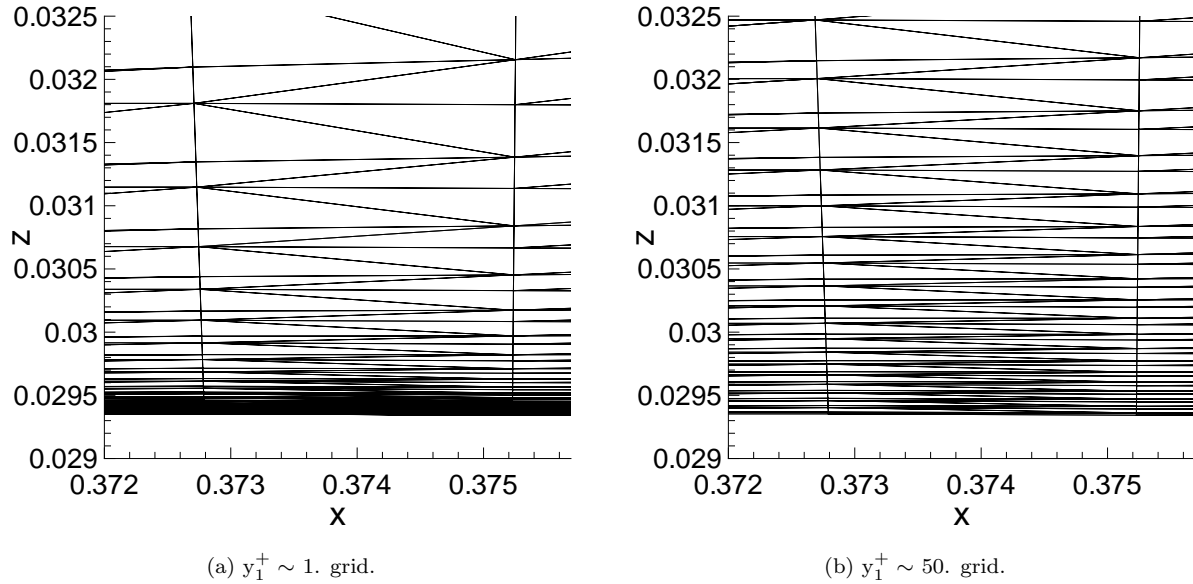


Figure 21: Detail of slice through the grid, $x/c \sim 0.374$, $\eta = 0.25$, ONERA M6 wing.

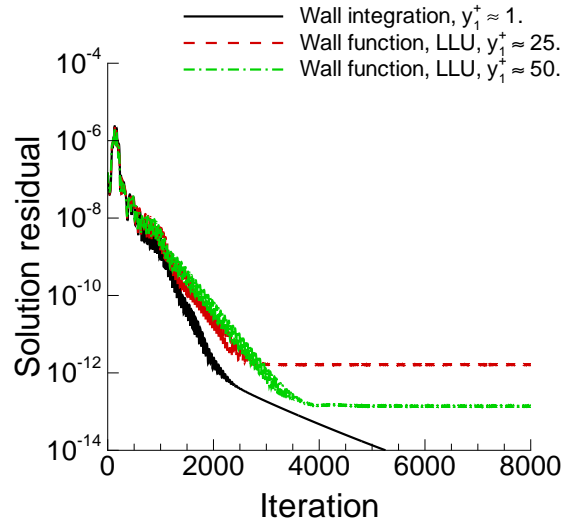
calculations accurately placed the location of the shock on the wing. Relatively good agreement of pressure coefficient distributions occurred at $\alpha = 4.08^\circ$ degrees, though the shock location moved slightly upstream with the wall function grids.

Surface streamlines for the wall integration, $y_1^+ \approx 1$, and wall function, $y_1^+ \approx 25$, at $\alpha = 4.08^\circ$ degrees are plotted in Fig. 24. Strong cross-flow occurs on the outboard region of the wing, as seen by the streamlines moving outboard, toward the wing tip, downstream of the upper surface shock. The SA wall model on the $y_1^+ \approx 25$ grid, to some degree, mimicked the wall integration streamlines. The SST wall model on the same grid did not show nearly the outward turning. The surface streamlines are calculated from the average velocities in the elements in the grid attached to the wing boundary. Wall integration grids, with wall spacing of 5 wall units or less, are assumed to provide a reasonable representation of the surface flow. It is questionable whether wall function grids can, in general, provide the correct average velocity field. The further the boundary element extends beyond the viscous sub-layer, the less linear velocity profile is. Therefore the surface streamlines from wall function grids have some inherent error.

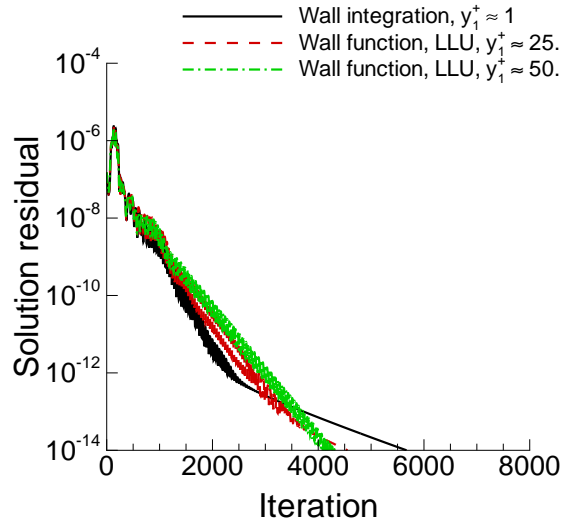
A summary of the lift, drag and pitching moments are listed in Tables 7 and 8. The pressure contribution to the lift and drag were fairly consistent between solutions obtained on the wall integration and the wall functions for both turbulence models and angles of attack. The viscous contribution to the drag computed by the wall function on the $y_1^+ \approx 50$ grid, though, was 40% below that of the wall integration viscous drag using the SA wall function model for both angles of attack. The SST wall function model computed similar viscous drag numbers as the SA model.

V. Summary

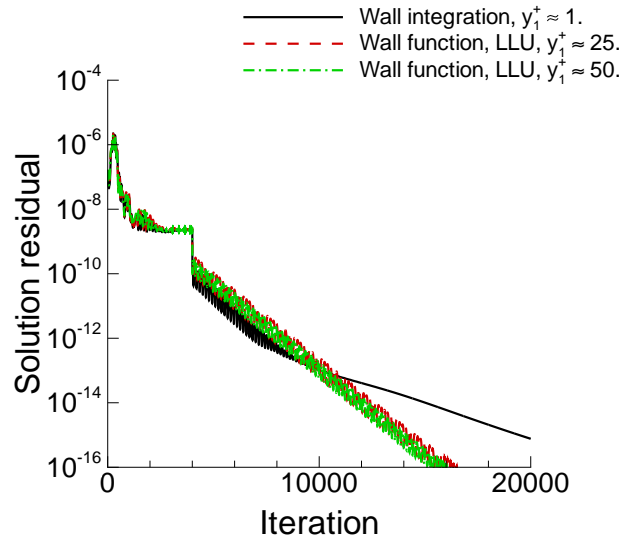
The implementation of two wall function models into the node-based unstructured-grid CFD code FUN3D has been described. The hybrid wall models of Knopp et al.,⁶ were used to simulate flow along a zero pressure gradient flat plate, an asymmetric diffuser, a 2D airfoil and a 3D semi-span wing. Reasonable agreement with canonical and experimental data, comparing pressure and skin friction, was observed for the flat plate and asymmetric diffuser test cases. Computed friction velocity using log-layer packed type grids were more constant across a range of initial wall spacing for the flat plate. Log-layer unpacked type grids produced velocity, skin friction and pressure coefficient distributions very similar to those obtained with log-layer packed or wall integration grids for the RAE airfoil. The pressure distributions were close when comparing calculations using wall function grids and using the wall integration grids. The shock location and spanwise



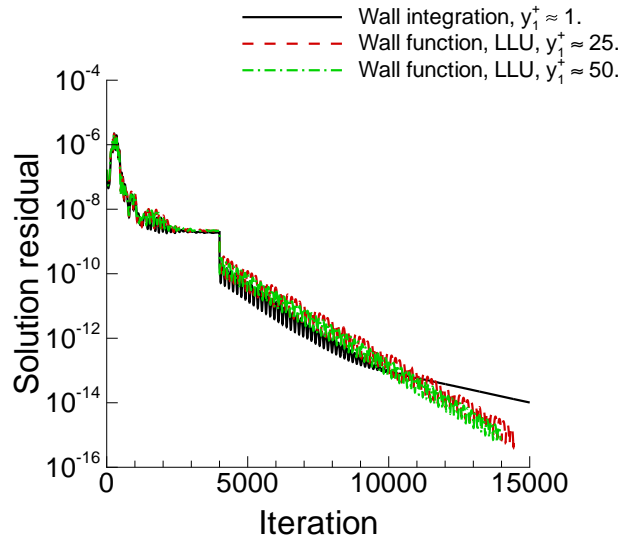
(a) SA turbulence model, $\alpha = 3.06^\circ$.



(b) SST turbulence model, $\alpha = 3.06^\circ$.



(c) SA turbulence model, $\alpha = 4.08^\circ$.

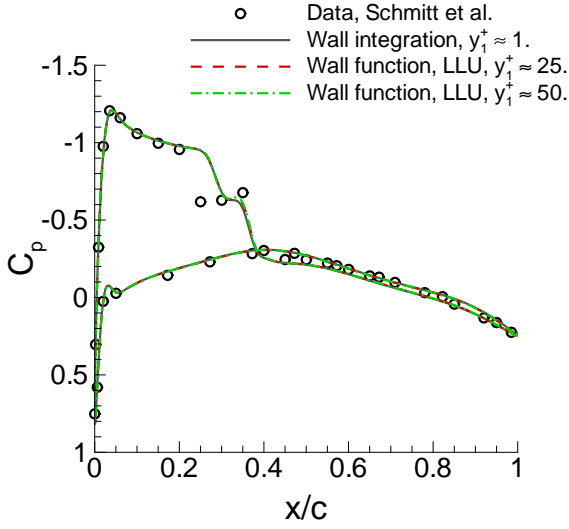


(d) SST turbulence model, $\alpha = 4.08^\circ$.

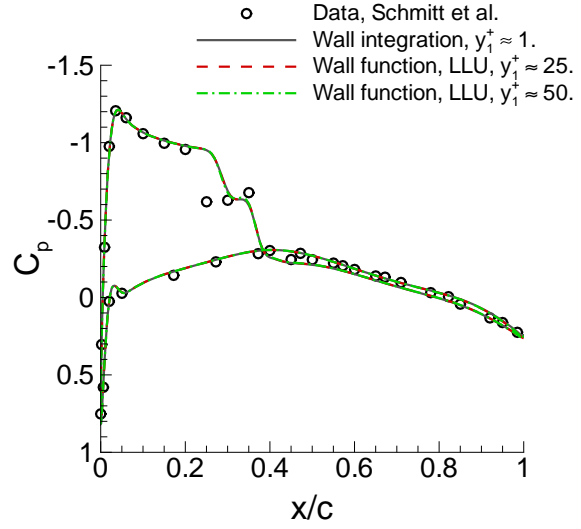
Figure 22: Solution residual, continuity equation, ONERA M6 wing.

Table 7: Computed forces and moments, ONERA M6, SA turbulence model.

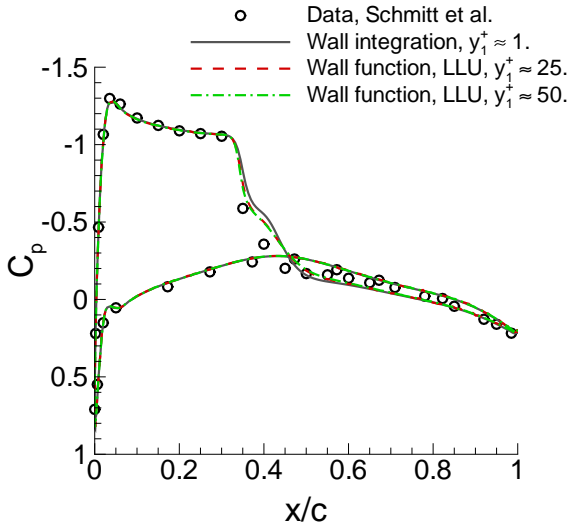
Grid	y_1^+	α deg.	Lift			Drag			Pitching moment
			total	pressure	viscous	total	pressure	viscous	
Wall integration	1.	3.06	0.260	0.260	0.000	0.0165	0.0116	0.0049	-0.180
Wall function (LLU)	25.	3.06	0.263	0.263	0.000	0.0155	0.0118	0.0037	-0.184
Wall function (LLU)	50.	3.06	0.264	0.264	0.000	0.0149	0.0118	0.0031	-0.184
Wall integration	1.	4.08	0.359	0.359	0.000	0.0266	0.0219	0.0047	-0.256
Wall function (LLU)	25.	4.08	0.354	0.354	0.000	0.0252	0.0218	0.0034	-0.251
Wall function (LLU)	50.	4.08	0.354	0.354	0.000	0.0246	0.0219	0.0027	-0.251



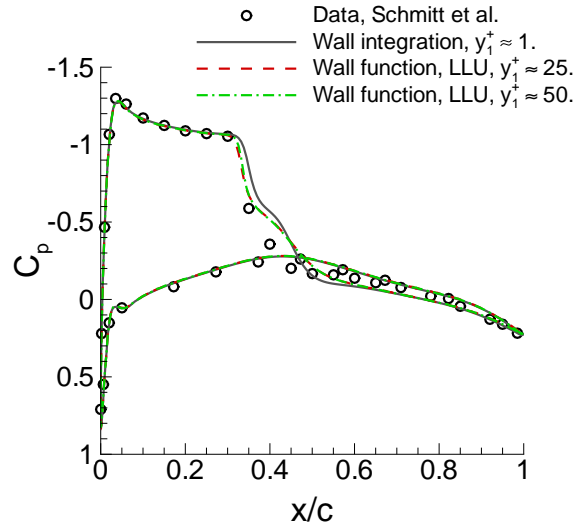
(a) SA turbulence model, $\alpha = 3.06^\circ$.



(b) SST turbulence model, $\alpha = 3.06^\circ$.



(c) SA turbulence model, $\alpha = 4.08^\circ$.

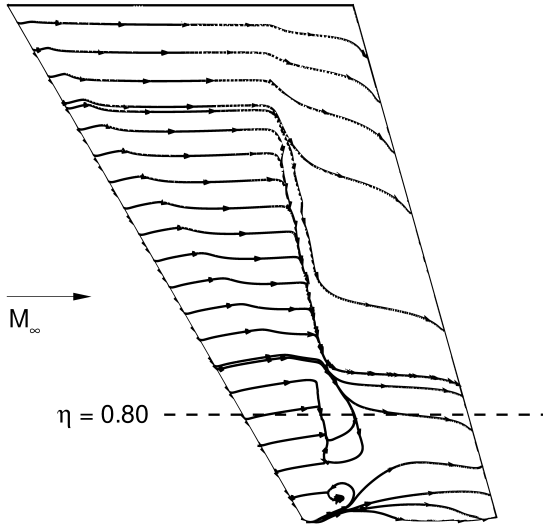


(d) SST turbulence model, $\alpha = 4.08^\circ$.

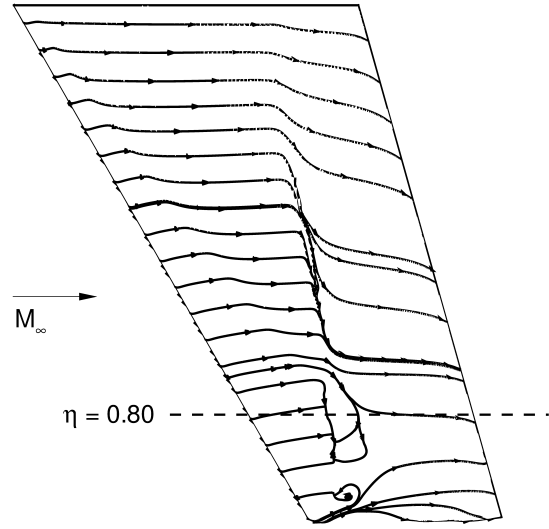
Figure 23: ONERA M6 wing, $\eta = 0.80$.

Table 8: Computed forces and moments, ONERA M6, SST turbulence model.

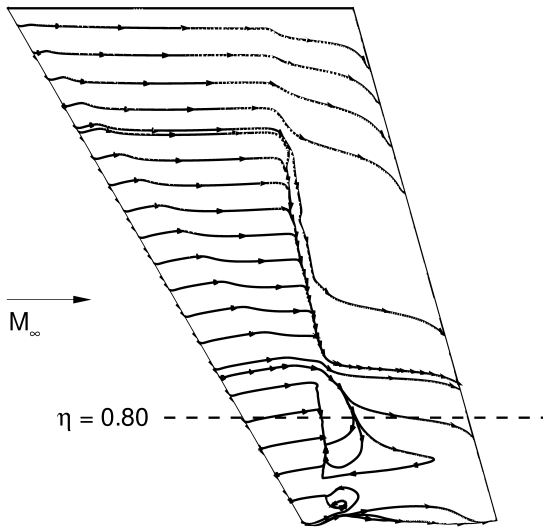
Grid	y_1^+	α deg.	Lift			Drag			Pitching moment
			total	pressure	viscous	total	pressure	viscous	
Wall integration	1.	3.06	0.264	0.264	0.000	0.0166	0.0116	0.0050	-0.184
Wall function (LLU)	25.	3.06	0.264	0.264	0.000	0.0153	0.0117	0.0034	-0.185
Wall function (LLU)	50.	3.06	0.264	0.264	0.000	0.0147	0.0117	0.0030	-0.184
Wall integration	1.	4.08	0.364	0.364	0.000	0.0268	0.0220	0.0048	-0.261
Wall function (LLU)	25.	4.08	0.353	0.353	0.000	0.0252	0.0218	0.0034	-0.249
Wall function (LLU)	50.	4.08	0.353	0.353	0.000	0.0247	0.0218	0.0029	-0.250



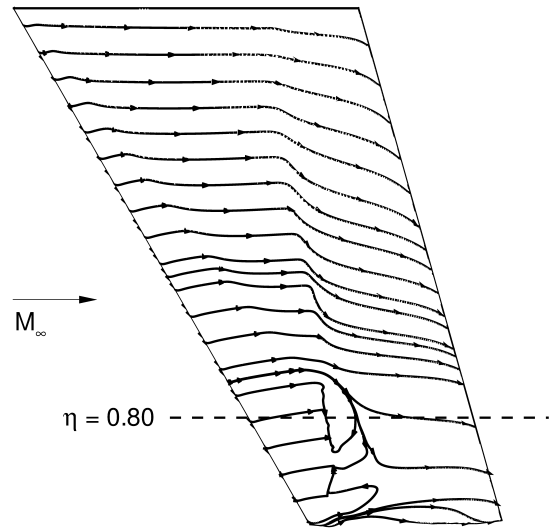
(a) SA turbulence model, $y_1^+ \approx 1$.



(b) SST turbulence model, $y_1^+ \approx 1$.



(c) SA turbulence model, $y_1^+ \approx 25$.



(d) SST turbulence model, $y_1^+ \approx 25$.

Figure 24: Upper surface streamlines, ONERA M6 wing, $\alpha = 4.08^\circ$.

flow features on the ONERA M6 wing were more difficult to calculate with the wall function models. The integrated viscous forces were off by 40% for the $y_1^+ \approx 50$ grid.

Acknowledgments

The authors would like to acknowledge the grids and advice from Elizabeth Lee-Rausch and Chris Rumsey of NASA-Langley Research Center, Hampton, Virginia, on obtaining the ONERA M6 solutions. Also, the authors would like to thank Neal Frink and Pieter Buning of NASA-Langley Research Center, Hampton, Virginia, for their insightful reviews of the paper. This work was sponsored by Revolutionary Computational Aerosciences under the Transformational Tools and Technologies project.

References

- ¹Lynch, C. E. and Smith, M. J., "Hybrid RANS-LES Turbulence Models on Unstructured Grids," AIAA Paper 2008-3854, June 2008.
- ²Spalart, P., "Detached-eddy simulation," *Ann. Rev. of Fluid Mec.*, Vol. 41, 2009, pp. 181–202.
- ³Esch, T. and Menter, F., "Heat transfer predictions based on two-equation turbulence models with advanced wall treatment," *Turbulence, Heat and Mass Transfer*, Vol. 4, 2003, pp. 633–640.
- ⁴Menter, F., Kuntz, M., and Langtry, R., "Ten Years of Industrial Experience with the SST Turbulence Model," *Turbulence, Heat and Mass Transfer*, Vol. 4, 2003, pp. 625–632.
- ⁵Kalitzin, G., Medic, G., Iaccarino, G., and Durbin, P., "Near-wall behavior of RANS turbulence models and implications for wall functions," *J. Comp. Phys.*, Vol. 204, 2005, pp. 265–291.
- ⁶Knopp, T., Alrutz, T., and Schwaborn, D., "A grid and flow adaptive wall-function method for RANS turbulence modelling," *J. Comp. Phys.*, Vol. 220, 2006, pp. 19–40.
- ⁷Spalart, P. R. and Allmaras, S. R., "A One-Equation Turbulence Model for Aerodynamic Flows," *Recherche Aerospatiale*, Vol. 1, 1994, pp. 5–21.
- ⁸Spalart, P. R., "Trends in Turbulence Treatments," AIAA Paper 2000-2306, June 2000.
- ⁹Menter, F. R., "Two-Equation Eddy-Viscosity Turbulence Models for Engineering Applications," *AIAA J.*, Vol. 32, No. 8, 1994, pp. 1598–1605.
- ¹⁰Allmaras, S. R., Johnson, F. T., and Spalart, P. R., "Modifications and Clarifications for the Implementation of the Spalart-Allmaras Turbulence Model," ICCFD7 1902, July 2012.
- ¹¹<http://turbmodels.larc.nasa.gov>, Accessed: 2015-03-01.
- ¹²Rumsey, C., Smith, B., and Huang, G., "Description of a Website Resource for Turbulence Model Verification and Validation," AIAA Paper 2010-4742, June 2010.
- ¹³Reichardt, H., "Vollständige Darstellung der turbulenten Geschwindigkeitsverteilung in glatten Leitungen," *Z. angew. Math. Mech.*, Vol. 31, No. 7, 1951, pp. 208–219.
- ¹⁴Spalding, D. B., "A single formula for the 'Law of the Wall'," *J. Appl. Mech.*, Vol. 28, No. 3, 1961, pp. 455–458.
- ¹⁵van Driest, E. R., "The problem of aerodynamic heating," *Aeronaut. Eng. Rev.*, Vol. 15, 1956, pp. 26–41.
- ¹⁶Roe, P. L., "Approximate Riemann Solvers, Parameter Vectors, and Difference Schemes," *J. Comp. Phys.*, Vol. 43, 1981, pp. 357–372.
- ¹⁷Batten, P., Clarke, N., Lambert, C., and Causon, D., "On the Choice of Wavespeeds for the HLLC Riemann Solver," *SIAM J. Sci. Comput.*, Vol. 18, 1997, pp. 1553–1570.
- ¹⁸Sun, M. and Takayama, K., "Artificially Upwind Flux Vector Splitting Scheme for the Euler Equations," *J. Comp. Phys.*, Vol. 189, 2003, pp. 305–329.
- ¹⁹Edwards, J., "A Low-Diffusion Flux-Splitting Scheme for Navier Stokes Calculations," AIAA Paper 1996-1704, May 1996.
- ²⁰van Leer, B., "Towards the Ultimate Conservative Difference Schemes V. A second order sequel to Godunov's Method," *J. Comp. Phys.*, Vol. 32, 1979, pp. 101–136.
- ²¹Roe, P. L., "Characteristic-Based Schemes for the Euler Equations," *Annu. Rev. Fluid Mech.*, Vol. 18, 1986, pp. 337–365.
- ²²Barth, T. and Jespersen, D., "The Design and Application of Upwind Schemes on Unstructured Meshes," AIAA Paper 1989-0366, Jan. 1989.
- ²³Venkatakrishnan, V., "Convergence to Steady State Solutions of the Euler Equations on Unstructured Grids with Limiters," *J. Comp. Phys.*, Vol. 118, 1995, pp. 120–130.
- ²⁴Anderson, W. and Bonhaus, D., "An Implicit Upwind Algorithm for Computing Turbulent Flows on Unstructured Grids," *Computers and Fluids*, Vol. 23, No. 1, 1994, pp. 1–22.
- ²⁵Anderson, W., Rausch, R., and Bonhaus, D. L., "Implicit/Multigrid Algorithms for Incompressible Turbulent Flows on Unstructured Grids," *J. Comp. Phys.*, Vol. 128, 1996, pp. 391–408.
- ²⁶<http://fun3d.larc.nasa.gov>, Accessed: 2015-03-01.
- ²⁷DalBello, T., Dippold III, V., and Georgiadis, N. J., "Computational Study of Separating Flow in a Planar Subsonic Diffuser," NASA TM-2005-213894, Oct. 2005.
- ²⁸Buice, C. U. and Eaton, J. K., "Experimental Investigation of Flow Through an Asymmetric Plane Diffuser," *J. Fluids Eng.*, Vol. 122, June 2000, pp. 433–435.

- ²⁹Cook, P. H., McDonald, M. A., and Firmin, M. C. P., "Aerofoil RAE 2822 - Pressure Distributions, and Boundary Layer and Wake Measurements," *Experimental Data Base for Computer Program Assessment. Report of the Fluid Dynamics Panel Working Group 04*, AGARD AR-138, May 1979.
- ³⁰Slater, J., Dudek, J., and Tatum, K., "The NPARC Verification and Validation Archive," ASME Paper 2000-FED-11233, June 2000.
- ³¹<http://www.grc.nasa.gov/WWW/wind/valid/raetaf/raetaf01/raetaf01.html>, Accessed: 2015-03-01.
- ³²Schmitt, V. and Charpin, F., "Pressure Distributions on the ONERA-M6-Wing at Transonic Mach Numbers," *Experimental Data Base for Computer Program Assessment. Report of the Fluid Dynamics Panel Working Group 04*, AGARD AR-138, May 1979.
- ³³Mani, M., Ladd, J., Cain, A., and Bush, R., "An Assessment of One-and Two-Equation Turbulence Models for Internal and External Flows," AIAA Paper 1997-2010, June 1997.
- ³⁴Wang, Q., Massey, S., and Abdol-Hamid, K., "Solving Navier-Stokes Equations with Advanced Turbulence Models on Three-Dimensional Unstructured Grids," AIAA Paper 1999-0156, Jan. 1999.
- ³⁵Anderson, W., Newman, J., Whitfield, D., and Nielsen, E., "Sensitivity Analysis for the Navier-Stokes Equations on Unstructured Meshes using Complex Variables," AIAA Paper 1999-3294, Nov. 1999.
- ³⁶Wong, P. and Zingg, D., "Three-Dimensional Aerodynamic Computations on Unstructured Grids Using a Newton-Krylov Approach," AIAA Paper 2005-5231, June 2005.
- ³⁷Chen, X., Zha, G., and Yang, M., "3D Simulation of a Transonic Wing Flutter using an Efficient High Resolution Upwind Scheme," AIAA Paper 2006-3216, June 2006.
- ³⁸Pirzadeh, S., "Three-Dimensional Unstructured Viscous Grids by the Advancing-Layers Method," *AIAA J.*, Vol. 34, No. 1, 1996, pp. 43-49.
- ³⁹Pirzadeh, S., "Advanced Unstructured Grid Generation for Complex Aerodynamic Application," AIAA Paper 2008-7178, Aug. 2008.